Screening of transition (Y, Zr, Hf, V, Nb, Mo, and Ru) and rare-earth (La and Pr) elements as potential effective dopants for thermoelectric GeTe – an experimental and theoretical appraisal

Bhuvanesh Srinivasan, Sylvain Le Tonquesse, Alain Gellé, Cédric Bourgès, Leo Monier, Isao Ohkubo, Jean-François Halet, David Berthebaud, Takao Mori

To cite this version:

Bhuvanesh Srinivasan, Sylvain Le Tonquesse, Alain Gellé, Cédric Bourgès, Leo Monier, et al.. Screening of transition (Y, Zr, Hf, V, Nb, Mo, and Ru) and rare-earth (La and Pr) elements as potential effective dopants for thermoelectric GeTe – an experimental and theoretical appraisal. Journal of Materials Chemistry A, 2020, 8 (38), pp.19805-19821. 10.1039/d0ta06710e . hal-02991418

HAL Id: hal-02991418

https://hal.science/hal-02991418

Submitted on 9 Nov 2020

Screening of Transition (Y, Zr, Hf, V, Nb, Mo, Ru) and Rare-earth (La, Pr) Elements as Potential Effective Dopants for Thermoelectric GeTe – an Experimental and Theoretical Appraisal

Bhuvanesh Srinivasan,[a,b] Sylvain Le Tonquesse,[b] Alain Gellé,[c] Cédric Bourgès,[a] Leo Monier,[b] Isao Ohkubo,[a] Jean-François Halet,[b,d] David Berthebaud,*[b] Takao Mori*[a]

[a] *WPI International Center for Materials Nanoarchitechtonics (WPI-MANA), National Institute for Materials Science (NIMS), 1-1 Namiki, Tsukuba 305-0044, Japan*

[b] *CNRS-Saint Gobain-NIMS, UMI 3629, Laboratory for Innovative Key Materials and Structures (LINK), National Institute for Materials Science, 1-1 Namiki, Tsukuba 305-0044, Japan*

[c] *Univ. Rennes, CNRS, IPR – UMR 6251, F-35000 Rennes, France*

[d] *Univ. Rennes, CNRS, Institut des Sciences Chimiques de Rennes (ISCR) – UMR 6226, F-35000 Rennes, France*

* **Correspondences**: David.BERTHEBAUD@cnrs.fr (D.B); MORI.Takao@nims.go.jp (T.M)

† Electronic Supplementary Material (SI) available

Abstract

GeTe, which undergoes phase transition between low symmetric rhombohedral to high symmetric cubic phase between 550 – 700 K (depending on the dopant and composition) and its alloys have widely been considered as promising candidates for mid-temperature range thermoelectrics. A variety of dopants have been tried in the past to improve further the thermoelectric performance of GeTe. In this work, an extensive experimental- and theoretical-based screening of transition (Y, Zr, Hf, V, Nb, Mo, and Ru) and rare-earth elements (La, Pr) that were not used in the past, are studied to explore if they can be of any potential use as dopants in thermoelectric GeTe. Out of these studied dopants, Ru, Nb, Pr, V, and Mo were found to be detrimental, Y and Hf to be reasonable, and Zr and La to be more promising. The transition or rare-earth dopant dependent variation in transport properties and thermoelectric performance of GeTe is corroborated with a concoction of factors ranging from modifications of the band gap, energy difference between the two valance band maxima, magnetic character, nature of the dopant or impurity state and their position with regard to the Fermi level, secondary cubic GeTe phase, *etc*. Contrary to the classical approaches where intrinsic Ge vacancies (that are inherently formed due to the thermodynamic nature of GeTe) are suppressed to improve their thermoelectric performance, an opposite approach is adopted in this work. Here by intentionally creating more electrically dormant Ge vacancies and modulating/balancing it with Zr-doping, an improved figure of merit, *zT* ~1.3 at 673 K is obtained for Ge-deficient $Ge_{0.98}Zr_{0.005}Te$ compound, thanks to the suppression of the lattice contribution to the thermal conductivity arising due to the large density of planar defects in these vacancy-induced compounds. These optimized Ge-deficient Zr-doped materials when codoped with Sb, results in effective convergence of electronic band valleys by tuning the crystal field effect and reduced thermal transport, thus yielding a high *zT* ~1.8 at 723 K. This work not only screens a directory of dopant elements to enrich the current state of the knowledge on GeTe-based compounds, but also indicates that the strategy of creation and synchronization of Ge-vacancies with a certain dopant is an alternative and effective route for enhancing *zT*.

Keywords: *Thermoelectrics; GeTe; Zr-doping; defects; band engineering*

1. Introduction

Energy sustainability is one of the major key technological challenges in this 21st century. Growing awareness and alarming concern for the environment and renewable energy supplies has revitalized advances in materials engineering and technologies for energy conversion in recent years. Thermoelectric (TE) devices with their potential to reversibly convert waste heat into useful electricity propound the likelihood of an all-solid-state technology for power generation, refrigeration, temperature stability, and control.[1–4] The TE material's performance is evaluated in terms of a dimensionless figure of merit, $zT = S^2\sigma T/\kappa$ where S, σ, T and κ are the Seebeck coefficient, electrical conductivity, absolute temperature and total thermal conductivity (sum of the electronic contribution, κ_e, and the lattice contribution, κ_{latt}), respectively. Boosting the TE power factor ($S^2\sigma$) and/or suppressing the thermal transport (κ) are the key paradigm to realize high zT. Utilizing phononic scattering mechanism, that is achieved via nanostructuring, which includes the engineering of nanoscale defects (dislocations, stacking faults, point defects, nanopores), and multiscale hierarchal architecting,[5–9] imparting rattling impurities,[10] intrinsic bond / strong lattice anharmonicities,[11–13] *etc*., to suppress thermal transport (κ_{latt}) is a well-known strategy to enhance zT. However, the electrical transport properties, S and σ are interrelated *via* carrier concentration, but in a contrary way (as per Pisarenko's relation) and confront a bigger challenge in improving the power factor, paramount for better energy conversion efficiency. In the last decade, this issue has been masterly addressed with the revitalization of the 'band structure engineering' approach, which encompasses electronic band convergence,[14,15] fostering resonance states or local distortion of the density of states (DOS) near the Fermi level (by impurity atoms),[16] quantum confinement of charge carriers,[17] nestification,[18] electron filtering effect,[19,20] dimensionality reduction,[21] modulating light bands with low effective mass,[22] deformation potential coefficient,[23] blocking of minority charge carriers,[24,25] which effectively helped in decoupling S and σ to a certain extent. Even the ideas such as the utilization of magnetic effect,[26–29] partial crystallization of semiconducting chalcogenide glasses (based on phonon-glass electron-crystal approach)[30–34] and processing techniques like Hybrid Flash-SPS techniques[35–37] were explored with notable degrees of success.

This concept of band engineering has been effectively used to tune the TE properties in various *p*- and *n*-type materials such as PbTe,[38,39] SnTe,[40–43] Mg_2Si,[44] half-Heusler,[45] *etc*. In this category of mid-temperature range TE candidates, GeTe has gained prominence in the past few years. It exists in a rhombohedral crystal structure (*r*-GeTe) and turns into a cubic structure (*c*-GeTe) at ~700 K.[46] Due to higher valley degeneracy, the TE performance is known to maximize at the cubic high symmetric domain[35,47] and hence, reducing the phase transition temperature can boost/stabilize the TE performance over a broad temperature range. Though this has been the general norm/convention with GeTe, there have also been recent studies where high TE performance were reported even for the low temperature *r*-GeTe, because of the convergence of split band valleys derived from the rhombohedral distortion.[48–50] Generally, the high carrier concentration (in the order as high as ~10^{21} cm^{-3}) due to the low formation energy of Ge vacancies in pristine GeTe affects the TE performance in this *p*-type highly degenerated semiconductor,[46,51] thus it is essential to optimize the charge carrier level to improve the TE performance in GeTe. Besides the high carrier concentration and phase transition, the presence of multiple valence bands in GeTe, provide these *p*-type intriguing materials with diverse degrees of freedom to play and tune their transport properties.[52] Some of the earlier reported approaches for GeTe-based materials to improve their electrical transport and/or to reduce the thermal transport have been adopted on single dopant containing compositions such as $Ge_{1-x}Pb_xTe$,[53] $Ge_{1-x}Bi_xTe$,[54] $Ge_{1-x}In_xTe$,[55] $Ge_{1-x}Ga_xTe$,[35] $Ge_{1-x}Cr_xTe$,[56] $Ge_{1-x}Ti_xTe$,[57] $Ge_{1-x}Al_xTe$,[58] $GeTe_{1-x}Se$,[59] $Ge_{1-x}Sb_xTe$,[60,61] $Ge_{1-x}Ag_xTe$,[62] $Ge_{1-x}Mn_xTe$,[63,64] LiI-GeTe,[65] *etc*., where the zT_{max} value generally ranged between 1.0 – 1.5 in most of these singly doped cases. Similarly, many co-doped compositions such as GeTe-$AgSbTe_2$ (TAGS),[66] GeTe-

$AgInTe_2$,[67] GeTe-$LiSbTe_2$,[68] $(GeTe)_nSb_2Te_3$,[69] $Ge_9Sb_2Te_{12-x}$,[70] GeTe-$AgSbSe_2$,[71] $(Bi_2Te_3)_nGe_{1-x}Pb_xTe$,[72] $Ge_{1-x}Sb_xTe_{1-y}Se_y$,[73] $Ge_{1-x-y}Sn_xPb_yTe$,[74] GeTe-GeSe-GeS,[75] $Ge_{1-x-y}Bi_xIn_yTe$,[76,77] $Ge_{1-x-y}Bi_xSb_yTe$,[47] $Ge_{1-x-y}Pb_xBi_yTe$,[48] $(Ge_{1-x}Dy_xTe)_y(AgSbTe_2)_{1-y}$,[78] $Ge_{1-x-y}Cd_xBi_yTe$,[79] $Ge_{1-x-y}Ga_xSb_yTe$,[35] $Ge_{1-x-y}Pb_xSb_yTe$,[49] $(Ge_{1-x}Yb_xTe)_y(AgSbTe_2)_{1-y}$,[80] $Ge_{1-x-y}Sb_xZn_yTe$,[81] $Ge_{1-x-y}Mn_xBi_yTe$,[63,82] $Ge_{1-x-y}Mn_xSb_yTe$,[63] $Ge_{1-x-y}P_xSb_yTe$,[83] $(Ge_{1-x}Dy_xTe)_y(AgSbTe_2)_{1-y}$,[80] and more recently $Ge_{1-x-y}Cr_xBi_yTe$[56] and $Ge_{1-x-y}Ti_xBi_yTe$[57] show zT_{max} values generally ranged between 1.5 – 2.0 or even more for some compositions.

The interesting TE results obtained from the aforementioned compositions, especially the couple of recent findings on transition metal (Ti and Cr) doped GeTe,[56,57] trigger us to further explore some of the other rarely studied transition metals like Y, Zr, Hf, V, Nb, Mo, and Ru, and rare-earth metals like La and Pr as potential dopant candidates for GeTe. A thorough experimental screening of these elements is accompanied with theoretical computations to understand how the addition of these transition and rare-earth elements can influence the electronic band structure (and thus the resulting TE properties) of GeTe. In most general cases, pristine GeTe exhibits zT ~0.85 at 700 K.[58,65] In this work, the strategy was that, if any of these transition or rare-earth elements doping to GeTe showed promising TE properties (*i.e.*, $zT > 1$), then they were optimized for their composition, and the resulting optimized compounds were finally codoped with Sb, which is widely reported to improve the band degeneracy in GeTe by reducing the phase transition temperature to produce more hole pockets.[35,47] In a nutshell, this work investigates the effect of doping a series of transition and rare-earth elements and their best performing optimized codoping (Zr-Sb) on the structural, electronic and thermoelectric properties of GeTe.

2. Materials & Methods

Reagents

Ge (Ingot, Rare metallic, 99.999 %), Te (Shot, Rare metallic, 99.999 %), Mo (Powder, Rare metallic, 99.9%), Nb (Powder, Wako, 99.9%), V (Turnings, Wako, 99.5%), Y (Ingot, Aldrich, 99.9%), Ru (Powder, Wako, 99.9%), Zr (Sponge, Aldrich, 99%), Hf (Turning, Wako, 99.9%), Pr (Turning, Wako, 99%), La (Turning, Wako, 99%) and Sb (Shots, Aldrich, 99.999%) were used for synthesis without any further purification.

Synthesis

The samples were synthesized using a vacuum-sealed tube melting process. Appropriate stoichiometric amounts of the starting elements were introduced into a quartz tube, and the ampoules that were sealed under a vacuum of ~2 x 10^{-3} mbar were then placed in a melting furnace and slowly heated to 1223 K for 8 hours, and then held at that temperature for 10 hours and finally cooled down to room temperature (~6 hours). Obtained ingots were hand crushed into powders, which were then consolidated by Spark Plasma Sintering (SPS-1080 – SPS Syntex Inc.) at 750 K (heating rate ~80 K/min) for 5 mins (holding time) with an axial pressure of ~60 MPa. After SPS processing, highly dense disk-shaped pellets were obtained with theoretical densities of > 98%. The sintered discs were then cut and polished to the required shapes and dimensions for various thermoelectric measurements.

Powder X-ray diffraction

Powder X-ray diffraction (PXRD) patterns were recorded at room temperature in the 2θ range of 10^o – 90^o using Rigaku Smart Lab 3 diffractometer (Cu radiation, $\lambda_{K\alpha1} = 1.5418$ Å, and $\lambda_{K\alpha2} = 1.5444$ Å in a ratio $\lambda_{K\alpha2} / \lambda_{K\alpha1} = 0.5$) with a step size of 0.02^o and a scan speed of 2^o/min. Le Bail refinements were performed using the WinPLOTR software and the FullProf algorithm.[84–86] The shape of the diffraction peaks was modeled using a Thompson–Cox–Hastings pseudo-Voigt profile function.[87] Zero-point shift, peak shape, and lattice parameters were systematically refined, and the background contribution was fitted using a 6-order polynomial. More realistic estimated standard deviations were calculated using the Bérar method.[88]

Electrical and thermal transport

The Seebeck coefficient and electrical resistivity were measured simultaneously on ~2×2×9 mm^3 bars using a commercial instrument (ZEM-2, ADVANCE RIKO Inc.) under partial pressure of He.

The temperature-dependent thermal diffusivity, D, was measured using the laser flash diffusivity method in LFA-467 Hyperflash (Netzsch) on graphite coated disc-shaped samples of ~10 mm diameter and ~2 mm thickness. The temperature-dependent heat capacity, C_p, was derived using a standard sample (pyroceram-9060) in LFA-467, which is in good agreement with the Dulong–Petit C_p value. The total thermal conductivity was calculated using the formula $\kappa = D \times C_p \times \rho$, where ρ is the density of the sample (measured using Archimedes' principle). In some cases, to better understand the thermal transport properties, the contributions from electronic and lattice parts were calculated. The lattice thermal conductivity (κ_{latt}) was estimated from κ by subtracting the electronic contribution (κ_e) *via* the Wiedemann-Franz law, as in the following equation,

$$\kappa_e = L\sigma T \qquad (1)$$

where L is the Lorenz number computed by the condensed version of Single Parabolic Band model with acoustic phonon scattering (SPB-APS)[89], as in the following equation,

$$L = 1.5 + \exp\left[-\frac{|S|}{116}\right] \qquad (2)$$

where the Lorenz number (L) is in 10^{-8} $W\Omega K^{-2}$ and the Seebeck coefficient (S) is in $\mu V K^{-1}$.

The uncertainty in the results for the values of electrical and thermal transport properties was ~5% and ~7%, respectively, and for the overall zT was ~ 12%.[90] To increase the readability of the figures, the error bars are not shown in the figures.

Computational procedures

First-principles calculations using Density Functional Theory (DFT) were performed to understand the effect of transition metal and/or rare-earth dopants on the electronic states of GeTe. The projector-augmented-wave (PAW) approach[91] implemented in the Vienna ab initio simulation package (VASP)[92] was used. Computations were performed using the generalized gradient approximation (GGA) for the exchange-correlation term parameterized in the Perdew–Burke–Ernzerhof functional.[93] Spin-orbit coupling (SOC) was included in the calculations.

Calculations were performed on cubic structural models, as we were interested in the high-temperature behavior of doped GeTe compounds. Dopants were substituted for Ge atom in a 4 × 4 × 4 super-cell ($MGe_{63}Te_{64}$ cubic models; M = transition / rare-earth element). Similar to the work of Hoang *et al.* on the impurity clustering in GeTe,[94] we chose a cluster made of one M atom surrounded by 6 Sb atoms (Sb and M atoms were placed far from each other in the supercell) for the M-Sb codoped GeTe composition ($Sb_6MGe_{57}Te_{64}$). In all the calculations, the positions were fully relaxed. For Ru doping, calculations using the GGA + U + (J) method were also carried out with Hubbard value $U = 2$ eV and Hund value $J = 0.5$ eV).[95,96] Almost no differences were found compared to the GGA calculations, hence only the results obtained from GGA calculations will be presented in the article.

3. Results & Discussion

Firstly, the primary motive is to figure out which among the planned transition elements (Nb, Y, Hf, Zr, Ru, Mo, V) and rare-earth elements (Pr, La) as dopants can potentially improve the TE performance in GeTe. Considering the fact that in most general cases the pristine GeTe exhibits $zT_{\max}$ ~0.85 at 700 K, the threshold that we set here to consider that transition / rare-earth dopant to be of any potential benefit for GeTe thermoelectrics, only if the zT exceeds 1 in those doped compositions. In order to shortlist the potential candidate among Nb, Y, Hf, Zr, Ru, Mo, V, Pr, and La, a small proportion of each of the element was doped to GeTe. Depending on their oxidation states, the doping level was fixed at either 2 mol% (for elements with 2^+ or 3^+ oxidation state like La, Y, V, Ru) or 0.5 mol% (for elements with 4^+ oxidation state like Zr, Hf).

Structural analysis

PXRD results for the pristine GeTe, $Ge_{0.08}Y_{0.02}Te$, $Ge_{0.995}Hf_{0.005}Te$, $Ge_{0.995}Mo_{0.005}Te$, $Ge_{0.98}V_{0.02}Te$, $Ge_{0.995}Zr_{0.005}Te$ and $Ge_{0.98}La_{0.02}Te$ compositions are presented in Figure 1. In all cases, the sharp reflections from PXRD indicated the high crystallinity of the SPS processed samples. The major reflections from the PXRD pattern could be indexed to a rhombohedral GeTe phase ($R3m$ space group, lattice parameters, a ~ 4.165 Å, and c ~ 10.670 Å), which was confirmed further with the presence of double reflections [(024) and (220)] in the range of 2θ values between 41° to 44° in $Ge_{1-x}M_xTe$ (M = transition / rare-earth element; $x = 0.02$ or 0.005). Besides the low-temperature rhombohedric GeTe phase (main phase), a small amount of Ge impurities (cubic Ge, $Fd\overline{3}m$ space group, a ~ 5.656Å) were also observed for the majority of the samples. These minor cubic Ge reflections could be due to the thermodynamic nature of the GeTe, which is known to preferentially exist as a Te-rich composition.[47,50,62,97] Moreover, the formation energy of Ge vacancies is much lower (about just one-third) when compared to the formation energy of other 3 defects in GeTe, *i.e.*, Ge antisite, Te vacancy, and Te antisite, thus making it the most easily and favorably formed intrinsic defect.[98,99] In thermal equilibrium, Ge vacancies are the dominant defect for any Fermi level (E_F), even if Ge is the only carrier reservoir, and are envisaged to form impromptu for E_F ~0.25 eV above the valance band.[99] Generally, it is reported that this minor cubic Ge impurity phase in a small proportion in GeTe has no apparent detrimental influence on the TE performance.[50,62] Since rhombohedric GeTe is a faintly distorted rock-salt lattice along the [111] direction,[100,101] the impact of these doping elements on the crystal structure can be captured by the variation in lattice parameter and/or the α angle in the rhombohedral setting. The PXRD patterns of pristine and doped GeTe compounds were fitted by the Le Bail method[86] and their respective refined lattice parameters and α angles can be found in the Supporting Info (SI, Table S1). All these samples (pristine, Y, La, Zr, Hf, and Mo) have a fairly similar unit cell parameters, with a and c being 4.165 Å and 10.670 Å, respectively, and the hexagonal cell volume varying between ~160.2 – 160.5 Å^3. The only exception is the $Ge_{0.98}V_{0.02}Ge$ compound, which possessed a significantly smaller c = 10.573 Å, thus resulting in a slightly smaller unit cell volume of ~159.0 Å^3. This difference or stand out behavior of $Ge_{0.98}V_{0.02}Ge$ compound, when compared to other GeTe compounds presented here, is not just in terms of its crystallographic structural point of view, but also in terms of its electrical and thermal transport properties, which are discussed in the forthcoming section. PXRD results for the $Ge_{0.98}Ru_{0.02}Te$, $Ge_{0.98}Pr_{0.02}Te$ and $Ge_{0.98}Nb_{0.02}Te$ compositions are presented in Figure 2. In addition to the low-temperature rhombohedric GeTe main phase, these compounds that were doped with Ru, Pr and Nb also include a non-negligible amount of high-temperature cubic GeTe phase (space group $Fm\bar{3}m$). The presence of the secondary cubic GeTe phase in these compounds (Ru, Pr and Nb doped GeTe) can affect their TE transport properties, as observed earlier in the case of $Ge_{0.94}Ag_{0.06}Te$.[62] From the PXRD patterns, it is important to notice that Bragg peaks corresponding to the crystallographic plans normal or almost normal to the *c* direction are characterized by peak shape with larger tails, *i.e.* more Lorentzian characteristic, than other reflections. It affects the sample's diffraction pattern and is more prominent for the doped compositions, for example, for $Ge_{0.98}V_{0.02}Te$ compound than for undoped GeTe (SI, Figure S1). Such an effect, that is embodied by more Lorentzian feature, can be attributed to the presence of defects, which were already elucidated in detail (using HRTEM imaging) in several GeTe-based materials in the past.[51,102] The high values of the agreement factors (R_p, R_{wp}, χ^2) from the fitted patterns are due to the anisotropic peak broadening arising due to the defects in these GeTe compounds. These defects would significantly influence and play a key role in the thermal transport properties of these compounds.

Effects of V, Nb, Mo, Ru, and Pr on TE properties of GeTe

The TE transport properties of some of the transition-metal and rare-earth-doped GeTe compounds are presented in Figure 3. The short inference would be that the dopants V, Nb, Mo, Ru, and Pr were found to be detrimental to the thermoelectric properties of GeTe. Partially substituting these elements (V, Nb, Mo, Ru, and Pr) for Ge decreased their zT when compared to that of pristine GeTe (Figure 3e). Out of those, Ru was found to be the worst, followed by Nb, V, Pr, and Mo. Most of these dopants neither helped in significantly improving the power factor, $PF = S^2\sigma$ (Figure 3c) nor in suppressing the thermal transport (Figure 3d), thus resulting in a poor TE performance. The only exemption is the V-doping, which substantially decreased the thermal transport, however, the PF was adversely affected, thus offsetting the effect of suppressed κ.

To have a more cogent understanding of the impact of these transition and rare earth dopants on the electrical transport properties in GeTe, DFT calculations were performed. These DFT calculations were carried out on 4 x 4 x 4 supercells derived from the cubic structural arrangement of GeTe (high-temperature phase). The electronic densities of states (DOS) computed for the cubic models of V, Nb, Mo, and Ru-doped compounds are presented and compared with undoped *c*-GeTe in Figure 4. Their electronic band structures were also computed and analyzed, aiming to provide some insight into how the valence band structure is modified upon doping. The band structures are plotted in Figure 5 along some high symmetry lines of the cubic Brillouin zone (BZ). The band gap (E_g) at L-point for pristine *c*-GeTe was calculated to be 226 meV, in agreement with the previous reports.[35,47,58,103] The DOS calculations (Figure 4a-d), which shows the shift of the Fermi level away from the valence band (*i.e.*, upwards / toward the conduction band) in the case of Nb and Mo doping, clearly suggests the suppression of the *p*-type charge carriers (holes) with the substitution of these dopants. It must be noted that the E_g mentioned here and throughout this paper, corresponds to the energy difference between the Te and the Ge bands at the L-point. When there is no intruder state (*i.e.*, dopant/impurity state) in the gap, it corresponds to the vertical gap at the L-point. Since the variation of this value reflects the difference in the energy gap between Te and Ge bands, it is more suitable to interpret the changes in the electrical properties. Band structure computations show that for the cases of Ru, Mo, and V doping, intruder states are present in the gap (Figures 5d-f). According to the perturbation theory (PT), the intruder states are defined as correction functions having energy (eigenvalue of H_0) close to the reference energy $E_m^{(0)}$, thus causing convergence problem in the perturbation summation, thus being branded as an Achilles' heel in multireference PT.[104,105] In the case of V-doped GeTe, the intruding V-bands are flat and localized within the bandgap (Figure 5f). The band gap at the *L*-point, without considering the intruder states, has increased from 226 meV to 250 meV when compared to the pristine *c*-GeTe. This can explain the reduction in its electrical conductivity (Figure 3a). V-doping modifies and distorts the DOS with respect to that of GeTe, as it seems to have induced resonance states (marked by the presence of a sharp hump), adjacent to E_F (Figure 4d). The presence of such resonance levels near E_F can help to increase *S* (as per Mott's relationship), like in the present case, as V-doped GeTe stands out in terms of thermopower (at least in the lower temperature domain) when compared to any other compositions presented here. This standout behavior is not just in terms of their transport properties, but also from the crystallographic point of view, where they possessed a significantly smaller $c = 10.573$ Å, thus resulting in a slightly smaller unit cell volume of ~159.0 Å^3, and a reduced c/a ratio of 2.537. At the same time, it must be noted that too much distortion of DOS near E_F can affect the carrier mobility, and this adds up to the reasons for this V-doped GeTe exhibiting poor σ. Had these resonance states been more close, *i.e.*, at the vicinity of E_F (instead of being adjacent), then there could have been a much significant beneficial impact on the thermopower, as in the case of previously reported In-doped GeTe.[55] Such impurity states are also induced for Ru-doped GeTe and Mo-doped GeTe, but they are less likely to make any gainful influence on the thermopower, as they are not present close to the proximity of E_F. For both Mo and Ru-doped GeTe, a part of the impurity states are localized near the top of the valence band and another part expands in the whole valence band. Compared to 3*d* orbitals of V, the 4*d* orbitals of Mo and Ru are more coupled to the *p* orbitals of Te. For Mo-doped GeTe and V-doped GeTe, besides the presence of intruder states, the first-principles calculations performed and reported here reveal some magnetic characters, *i.e.*, DOS calculations yielded non-zero total magnetization. Though the introduction of magnetic ions (albeit with very careful tuning of the composition) have recently been shown to boost the power factor by balancing between improved effective mass (m^*) and reduced mobility (μ) in certain specific compounds like $CuGaTe_2$, Bi_2Te_3, SnSe,[8,29,106] it seems not to be the case here in GeTe. Previous spin-polarized band structure computations have proved that the introduction of magnetic ions in GeTe will induce spin scattering, which in turn will negatively affect the carrier mobility in these compounds. Typically, if the carrier density is optimized, then it is the weighted mobility $\mu_W = \mu(m^*/m_0)^{3/2}$, where m_o is the free electron mass, that governs the maximum thermoelectric power factor in a given material. Apart from the variety of reasons explained above (such as the presence of intruder states, large E_g, heavy DOS distortion), this magnetic contribution (and thus the low μ) adds up to explain why V-doped GeTe has exhibited poor *PF*, which is least among the studied materials here (Figure 3c). The high resistivity resulting from V-doping has resulted in reduced κ (Figure 3d), mainly due to the largely suppressed electronic contribution, κ_e. Given that the Mo-doping (with some predicted magnetic interactions) did not affect *PF* as badly as V-doping, in fact showing comparable *PF* as that of pristine GeTe sample (Figure 3c), there is a possibility to improve *PF* further in Mo-doped GeTe by playing with this interaction between carriers and magnetic moments *via* composition tuning to achieve a better trade-off between m^* and μ, thus throwing an interesting aspect for potential future work. However, the calculations predicted the Ru atom to be non-magnetic with a d^6 electronic configuration. This is coherent with the crystal field theory in octahedral symmetry, where the t_{2g} orbitals are fully occupied. GeTe band structure manifests a second maximum of the valence band in the $\Gamma \rightarrow K$ (Σ) direction. The energy separation between these light and heavy hole valence bands ($\Delta E_{L\Sigma}$) for undoped *c*-GeTe was found to be 64 meV, in agreement with the literature report.[103] This energy difference ($\Delta E_{L\Sigma}$) for high-temperature *c*-GeTe is much lower than that of the low-temperature *r*-GeTe ($\Delta E_{L\Sigma}$ = 150 meV).[103] This is beneficial and is consistent with the fact that the temperature increases the band convergence in GeTe. In the case of Nb and Ru doping, the negative value of the energy separation between the two valence bands, $\Delta E_{L\Sigma}$ (Table S2, SI), indicates that the heavy hole band is larger in energy than the light hole band (it can be seen from Figures 5c, d). Nb states are located just at the bottom of the conduction band. The higher κ in Ru, Nb and Pr-doped GeTe samples can be attributed to the presence of a significant proportion of secondary cubic GeTe phase, as mentioned in the previous section and shown from the PXRD patterns given in Figure 2. Such high symmetric cubic GeTe secondary phases are generally known to exhibit higher lattice thermal conductivity than the low symmetric rhombohedral GeTe main phase.[48] It is not a surprise that Ru-doped GeTe, with a culmination of aggregate effects (mostly negative on TE transport properties) such as the presence of intruder states, valence band divergence (hence lower S), secondary cubic GeTe phase (higher κ_{latt}), languishes at the bottom as the least thermometrically performing material (least zT) among the transition and rare-earth element doped GeTe compounds that are reported in this work (Figure 5e).

Effects of Y and Hf on TE properties of GeTe

Substitution of Y and Hf for Ge was found to be relatively promising, as they marginally improved zT in GeTe from ~0.85 at 723 K (for pristine case) to ~0.95 (Y-substituted) and ~0.98 (Hf-substituted) at 723 K (Figure 5e). In the case of Y-doping, the marginal improvement in zT is due to the suppressed thermal transport, while in the case of Hf-doping, it is due to the marginally improved power factor. Despite their slightly improved TE performance, Hf and Y-doped GeTe compounds exhibited $zT \leq 1$, hence they were not shortlisted for further experimental studies in this work. Of course, there is still some scope for further improvements with these Y and Hf dopants, if the compositions are properly optimized, presenting scope for future studies. DFT results show that Y-doping does not change much the energy separation between the two valence band maxima (Figure 6c) when compared to that of pristine *c*-GeTe. The DOS results (Figure 6a) also shows that the projections arising from the Y-doping do not impart any change near E_{F} or near the top of the valance band or near the bottom of the conduction band, and instead, the dopant states arising from Y-doping seem to be buried deep within the conduction band. This explains why Y-doping did not influence the power factor values at high temperatures. Hf-doping to GeTe slightly tends to open up the band gap and tends to slightly decrease the energy separation between the two valence band maxima (Figure 6d), promoting band convergence and must explain their improved power factor (and hence the overall marginal improvement in zT). The values of E_{g} and $\Delta \mathrm{E}_{L\Sigma}$ for Hf-doped GeTe (Table S2, SI) are computed for the $\mathrm{HfGe_{63}Te_{64}}$ model, which has a much higher Hf-content than the experimental composition ($\mathrm{Ge_{0.995}Hf_{0.005}Te}$), so only the tendency has to be taken into account.

Effects of La and Zr on TE properties of GeTe

In the present study on transition and rare-earth elements as potential dopants for GeTe, La and Zr were found to be effective (Figure 7). Substituting La and Zr for Ge considerably enhanced $zT_{\max}$ of GeTe from ~0.85 at 723 K to ~1.1 at 673 K and 723 K, respectively, for La-doping and Zr-doping, as shown in Figure 7e. In both cases, *i.e.*, La-doping and Zr-doping, the thermal conductivity did not change much when compared to pristine GeTe (Figure 7d), however, the power factor was considerably improved (Figure 7c). Indeed, pristine GeTe exhibited a peak PF ~3.3 x 10^{-3} W/m.K^2 at 673 K, while it substantially increased for La-doped GeTe ($PF_{\max}$ ~4 x 10^{-3} W/m.K^2 at 673 K) and Zr-doped GeTe ($PF_{\max}$ ~4 x 10^{-3} W/m.K^2 at 723 K). From the band structure computations, the band gap at L-point increased from 226 meV for the pristine *c*-GeTe to 249 meV for the La-doped GeTe (Figure 8c). In the case of La-doping, the energy difference between the two valance band maxima remained unchanged when compared to that of pristine *c*-GeTe (69 meV). The impurity states arising from La are located far from E_{F} and seem to be buried deep within the conduction band of GeTe. Similar to that of La, doping Zr slightly opens up the band gap from 226 meV to 255 meV (Figure 8d). The energy difference between the two valence band maxima is also reduced to 53 meV (for 0.5 at.% Zr-doping) from 69 meV (undoped GeTe). Refer SI (Table S3) for the data extrapolation for 0.5 at.% Zr and for the band structure computed with a larger super-cell (Figure S3). This marginal convergence of the valence bands explains the improved *PF* in Zr-doped GeTe. As both La-doped GeTe and Zr-doped GeTe compounds exhibited $zT > 1$, they were shortlisted for further experimental studies. The upcoming sections in this paper will exclusively focus only on Zr-doped GeTe. The optimizations and codoping strategies with La-doped GeTe will be reported in future communication.

Ge-deficient *vs* stoichiometric Zr-doped GeTe

The next stage was aimed at optimizing the composition of Zr-doped compounds. 0.5 at% Zr-doping to GeTe ($Ge_{0.995}Zr_{0.005}Te$) boosted *zT* up to ~1.1 at 723 K. To find the optimum content of Zr to achieve the best *zT* in the GeTe-solid solution, experiments were carried out with varying Zr-content in the nominal composition $Ge_{1-x}Zr_xTe$ ($0.005 \leq x \leq 0.015$). Indeed, the $x = 0.005$ composition that exhibited the best *zT* in that series, as the addition of more Zr content did not have any significant improvement in the TE properties of GeTe. From the band structure computations, it is found that Zr-doping progressively increased the optical band gap and, at the same time, considerably reduced $\Delta E_{L\Sigma}$ (Table S3, SI). However, the effect of a large increase in E_g (thus lower σ) with higher Zr-content has negated the benefits of the converging trend of the valence bands. As altering the Zr-content did not yield any TE improvement, the next strategy was formulated with an aim at tuning the Ge-content to optimize the composition. By controlling the Ge-vacancy levels (by nearly making it vacancy-free), recent reports have shown some significant improvement in the TE performance in GeTe, thanks to the suppression of hole concentration and recovery of high carrier mobility.[50,51,107] In particular, Dong *et al.*,[50] has effectively demonstrated this strategy in Bi-doped Ge-excess $Ge_{1+x}Te$, where these excess Ge acted as a source to subdue the formation of Ge vacancies. In this work, a reverse strategy of Ge-deficient $Ge_{1-x+y}Zr_yTe$ compositions, where the aliovalent Zr can balance out or modulate the effects caused by Ge-deficiency was explored. For this purpose, the self-compensated samples of $Ge_{1-x}Zr_{0.005}Te$ ($x = 0.01 – 0.03$) were prepared. The self-compensated $Ge_{0.98}Zr_{0.005}Te$ ($x = 0.02$ in $Ge_{1-x}Zr_{0.005}Te$) was found to be the optimized composition. The TE transport properties of this Ge-deficient Zr-doped GeTe composition ($Ge_{0.98}Zr_{0.005}Te$) is compared with that of its stoichiometric counterpart ($Ge_{0.995}Zr_{0.005}Te$), as shown in Figure 9. Creating some small Ge-deficiency in the Zr-doped GeTe compound did not alter much the electrical transport properties, σ and *S* (Figure 9a-c) when compared to stoichiometric $Ge_{0.995}Zr_{0.005}Te$ compound. To understand this feature, the electronic structure and defect calculations (based on DFT) on GeTe, both on rhombohedral and cubic models that were meticulously computed and reported by Edwards *et al.*,[99] must be carefully analyzed. The simple model presented there for a Ge vacancy predicted one lesser *s* band and four fewer electrons in the valence bands.[99] The removal of each Ge atom will result in one empty valence band. The reported projected DOS near the Ge vacancy (for both rhombohedral and cubic arrangements) showed no new features in the gap. The new features that are rather present were buried beneath the valence band edge in the Te *s* and *p* bands. Since these defect states are found to be hyper-deep, the Ge-deficiency induced vacancies in GeTe are electrically and paramagnetically dormant. This can explain the fairly similar electrical transport properties between the $Ge_{0.98}Zr_{0.005}Te$ and $Ge_{0.995}Zr_{0.005}Te$ compounds. Moreover, the empty states resulting due to these Ge vacancies are not localized and they are virtually unperturbed states from the top of the valence band. The inconsequential defect relaxation energy was also reported to agree with the trivial charge localization around the vacancy,[99] and those empty states at the top of the valence band arising due to the inherently present Ge-vacancies, *i.e.*, intrinsic defects in GeTe (due to their thermodynamic nature), justifies the *p*-type metallic conduction in GeTe. This is further corroborated by the DFT calculations reported by Bayikandi *et al.*,[51] where the Fermi level moved down progressively into the valence band with increasing Ge vacancy levels; and in those Ge-vacancy models, the DOS contributions to the valence band were dominated by Te-5p^4 and Ge-4s^2 orbitals, while the majority contribution to the conduction band minima came from the Ge-4p^2 orbital. Imparting some Ge-deficiency in the Zr-doped GeTe composition, though did not affect much the overall electrical transport properties, *i.e.*, *PF*, it has influenced their thermal transport by notably decreasing the thermal conductivity (Figure 9d), especially the lattice contribution (Figure 9e). Such similar reduction in thermal transport with the introduction of cation deficiency has also been observed in the past for *n*-type Pb-deficient $Pb_{0.98-x}Sb_xTe$ compounds.[108,109] To explain this phenomenon in reduction in κ with the Ge-deficient Zr-doped $Ge_{0.98}Zr_{0.005}Te$ when compared to the stoichiometric $Ge_{0.995}Zr_{0.005}Te$, their structural results must be carefully introspected and compared. Le Bail fitted PXRD patterns of Ge-deficient $Ge_{0.98}Zr_{0.005}Te$ and stoichiometric $Ge_{0.995}Zr_{0.005}Te$ compounds are shown in Figure 10 and Figure S3 (SI), respectively, and their refined lattice parameters are shown in Table S4 (SI). The *a* and *c* lattice parameters of the two compositions are very similar. The major difference between the two diffraction patterns come from the peak shape of the Bragg reflections normal or almost normal to the [001] direction. In order to investigate this effect, several well-defined and non-overlapping Bragg peaks were fitted individually with a pseudo-Voigt function, $V_g(x)$. This function consists of a linear combination, $V_g(x) = \eta\ L(x) + (1-\eta)\ G(x)$, where $L(x)$ and $G(x)$ are the Lorentzian and Gaussian functions, while η is the refined mixing parameter and it shifts the profile more towards pure Gaussian or pure Lorentzian when approaching 0 or 1, respectively. Figure. 11 shows η and the full width at half maximum (FWHM) for several Bragg peaks of $Ge_{0.98}Zr_{0.005}Te$ and $Ge_{0.995}Zr_{0.005}Te$ patterns. In the case of stoichiometric $Ge_{0.995}Zr_{0.005}Te$, all the Bragg peaks were well fitted with η close to 1, which corresponds to pure Lorentzian peak shape. The result is similar in the case of Ge-deficient $Ge_{0.98}Zr_{0.005}Te$, except for the reflections (003), (104) and (105) which are better fitted with η abnormally larger than 1 corresponding to a 'super-Lorentzian' profile. Such index-dependent super-Lorentzian peak shapes are a clear indication of coherent planar defects in crystalline solids [110]. In the current scenario, other than the deformation of the peak shape, no notable dependence of the FWHM with the Miller indices is observed. In any case, the 'super-Lorentzian' profile for Ge-deficient $Ge_{0.98}Zr_{0.005}Te$ can be attributed to the presence of the planar-defects in GeTe, as already mentioned above. Lee *et al.*[102] showed using extensive TEM analyses that planar defects in GeTe are caused by the phase transition from the low-temperature rhombohedric to the high-temperature cubic phase. The phase transition can be described as an elongation of cubic unit cell, which can occur along with one of the four possible and equiprobable [111] directions, which will result in a complex 3D herringbone microstructure.[102] The diffraction pattern of such a complex crystal with a variety of defects is difficult to be simulated, as the current advanced programs can only handle 1D planar displacement [FAULTS program].[110,111] The deformation of Bragg peaks on the Ge-deficient $Ge_{0.98}Zr_{0.005}Te$ diffraction pattern seems to indicate a high density of defects for this composition. As the synthesis conditions were the same between these two samples (Ge-deficient $Ge_{0.98}Zr_{0.005}Te$ and stoichiometric $Ge_{0.995}Zr_{0.005}Te$), it seems likely that the higher density of defects in $Ge_{0.98}Zr_{0.005}Te$ is certainly related to the formation of Ge vacancies. Figure 11 clearly evidences the presence of the 'super-Lorentzian' profile only for the Ge-deficient $Ge_{0.98}Zr_{0.005}Te$ composition, pointing that Ge-deficiency has readily favored the formation of the larger density of planer defects in GeTe, than it would normally occur in the stoichiometric cases. This explains the lower lattice thermal conductivity in the Ge-deficient $Zr_{0.005}Ge_{0.98}Te$ when compared to that of its stoichiometric counterpart over the whole measured temperature range. The Ge-deficiency induced vacancy domains can create a barrier or hinder the flow of heat-carrying phonons of different mean free paths (MFP). The contrary approach adopted by Dong *et al.*,[50] where they used excess Ge ($Ge_{1+x}Te$) to suppress these vacancies resulted in an increasing tendency of κ_{latt} with excess Ge-content, thus the phonon scattering was reportedly weakened due to the lack of Ge vacancies and the resulting additional Ge precipitates also affected κ (as κ of pure Ge is much higher). The defect/vacancy induced a reduction in thermal conductivity has helped in conspicuously increasing zT in the Ge-deficient composition (Figure 9f). The Ge-deficient $Ge_{0.98}Zr_{0.005}Te$ compound exhibited a peak zT ~1.3 at 673 K, which is significantly higher when compared to that of the stoichiometric $Ge_{0.995}Zr_{0.005}Te$ composition (zT_{max} ~1.1 at 723 K) and to that of pristine GeTe (zT_{max} ~0.85 at 723 K). This strategy of intentionally creating more Ge vacancies may contradict the conventional approach (which is rather aimed at suppressing those intrinsic defects), it seems to work well for such transition metal-doped GeTe. These results further reinforce the very recent findings by Shuai *et al.*,[56] where such an opposite directional approach by decreasing the Ge vacancy formation energy (*i.e.*, the formation of more Ge vacancies and Ge precipitates) *via* another transitional metal (Cr) substitution at Ge site has also resulted in an improvement in *zT*.

TE properties of Zr and Sb codoped GeTe

To the optimized Ge-deficient $Ge_{0.98}Zr_{0.005}Te$ composition, 10 at.% Sb was codoped to form the Ge-deficient Zr-Sb codoped compound (*i.e.*, $Ge_{0.88}Zr_{0.005}Sb_{0.1}Te$). An improved band degeneracy has been widely reported in 8-10 at.% Sb doping in GeTe.[35,47,81,103] Hence Sb was codoped to the optimized Zr-doped GeTe intending to realize coadjutant synergistic band effects that would play a key role to ultimately boost the TE performance. The PXRD pattern of the Zr-Sb codoped $Ge_{0.88}$ $Zr_{0.005}Sb_{0.1}Te$ compound is presented in Figure 12. Le Bail lattice refined parameters (Table S5, SI) reveal that, with the insertion of Sb, the lattice parameter *a* increases from 4.166 Å for $Ge_{0.98}Zr_{0.005}Te$ to 4.199 Å for $Ge_{0.88}Zr_{0.005}Sb_{0.1}Te$. The other lattice parameter, *c*, however decreases from 10.661 Å for $Ge_{0.98}Zr_{0.005}Te$ to 10.530 Å for $Ge_{0.88}Zr_{0.005}Sb_{0.1}Te$. These changes in the lattice parameters have resulted in an expansion of the hexagonal unit-cell volume from 160.3 Å^3 for $Ge_{0.98}Zr_{0.005}Te$ to 160.8 Å^3 for $Ge_{0.88}Zr_{0.005}Sb_{0.1}Te$, which can be explained by Ge^{2+} being substituted by larger Sb^{3+} ions. It must be noted that the *c*/*a* ratio for pristine GeTe and $Ge_{0.98}Zr_{0.005}Te$ are ~2.56 and ~2.55, respectively, while it significantly reduces for $Ge_{0.88}Zr_{0.005}Sb_{0.1}Te$ (*c*/*a* ratio ~2.507). Such variations in the crystal field effect can notably influence the TE properties (by tuning the electronic band structures), as recently reported by some of us in the case of Ti-Bi codoped GeTe.[57]

The characteristic rhombohedral double reflections [(024) and (220)] in the range of 2θ values between 41^o to 44^o, got closer and almost merged when Sb was partially substituted for Ge in $Ge_{0.98}Zr_{0.005}Te$, as can be seen from the PXRD pattern in Figure 12. The evolution of the unit-cell parameters can be visually confirmed in the inset of Figure 12, which shows the displacement of the (105) and (006) reflections toward higher angles and (113) and (202) toward lower angles for $Ge_{0.88}Zr_{0.005}Sb_{0.1}Te$ when compared to the $Ge_{0.98}Zr_{0.005}Te$. Besides, an important broadening of the (006) and (105) peak shapes can also be observed (inset of Figure 12). This would indicate the formation of a much larger density of planar defects with the insertion of Sb in $Ge_{0.98}Zr_{0.005}Te$, which could play a critical role in influencing their thermal transport properties. However, no further in-depth peak profile analysis could be performed because of the overlapping of the important reflections.

The TE transport properties of the Zr-Sb codoped $Ge_{0.88}$ $Zr_{0.005}Sb_{0.1}Te$ are presented and compared with Ge-deficient $Ge_{0.98}Zr_{0.005}Te$ and pristine GeTe in Figure 13. The addition of Sb to Zr-GeTe extensively decreased the electrical conductivity, which is due to the suppression of the charge carriers arising due to the aliovalent donor dopant effect of Sb in GeTe. However, this reduction in σ is recompensated by the drastic rise in the *S* values (Figure 13b). The Zr-Sb codoped $Ge_{0.88}Zr_{0.005}Sb_{0.1}Te$ sample exhibited a high thermopower of ~125 µV/K at room temperature and a maximum of ~240 µV/K at higher temperatures, a notable improvement by 75% when compared to that of pristine GeTe and/or Zr-doped GeTe. First-principles calculations (DFT) can corroborate the reasons for this impressive rise in thermopower with Zr-Sb codoping. Computations with possible arrangements for the distribution of Sb atoms were carried out. However, the differences in the band structures between those structural arrangements were found to be small, and they showed consistent results (Figure 14 and Figure S5, SI). Quite significantly, Zr-Sb codoping in GeTe has resulted in the convergence of electronic band valleys by markedly shrinking the energy separation between the light hole and heavy hole valence bands, $\Delta E_{L\Sigma}$, to 21 meV, a sharp reduction by 70% when compared to the $\Delta E_{L\Sigma}$ of pristine *c*-GeTe, as shown in the band structure sketched in Figure 14. Codoping of Zr and Sb modifies the electronic band structure of GeTe by activating hole pockets at the bottom of the conduction band (refer to the DOS in Figure 14a). Zr-Sb codoping has resulted in adding donor states just below the conduction band. The exact position of E_F in these calculations should be slightly considered with caution, as these computations were based on stoichiometric GeTe (*i.e.*, without any Ge-vacancy). In any case, the band convergence would favor the raise in effective mass, m^* owing to the contributions from both the light and heavy hole bands (L and Σ bands) from the heavier effective mass near the E_F.[51,52] This phenomenon in a reduction in energy separation $\Delta E_{L\Sigma}$ by tuning the crystal field effect with the decrease of c/a ratio for Zr-Sb codoped is something that has also been observed for Ti-Bi codoped GeTe.[57] There is a slight change of trend or tendency with the electrical and thermal transport properties in Zr-Sb codoped $Ge_{0.88}$ $Zr_{0.005}Sb_{0.1}Te$ at ~573 K, which is an indication of the structural transition $R3m \rightarrow Fm\overline{3}m$. It must be noted that this structural transition for pristine GeTe occurs at around 673 K. Hence, codoping of Zr and Sb has stupendously reduced the phase transition temperature and readily increased the symmetric nature, which in turn will facilitate higher density of states effective mass (m^*_{DOS}) and weighted mobility. The Zr-Sb codoped $Ge_{0.88}Zr_{0.005}Sb_{0.10}Te$ sample exhibited κ ~1.5 W/m.K at room temperature, which accounted for a massive reduction by 360% when compared to that of pristine GeTe (κ~ 7 W/m.K at room temperature) and reduction by 300 % when compared to Ge-deficient $Ge_{0.98}Zr_{0.005}Te$ composition (κ ~6 W/m.K at room temperature). More importantly, the thermal conductivity remained low (between 1.5 – 1.2 W/m.K) throughout most of the measured temperature range. This ultra-low κ can be attributed to the synergistic suppression of both electrical (κ_e) and lattice (κ_{latt}) contribution to the thermal transport. The increased electrical resistance with the substitution of aliovalent Sb^{3+} for Ge^{2+} (and hence decreased carrier density), resulted in suppressed electronic contribution. The large density of planar defects, predicted by the PXRD results (Figure 12 and its inset), must have suppressed the transport of thermal phonons. This is consistent with a recent report on Sb-doping in GeTe,[107] where the presented HRTEM results showed a plethora of such planar defects, ranging from twinned and inter-twined planar domains, thickened herringbone domain boundaries, presence of stacking faults, interstitials all of which contribute to the scattering of phonons of a wider spectrum of mean-free paths. Hong *et al.* have established that Sb alloying in GeTe will alter the phonon dispersions, including the closing of the acoustic-optical phonon band gap, reducing the phonon group velocities and increasing the phonon-phonon scattering rates.[81] Importantly, Lee *et al.* observed ‘colonies’ of stacked herringbone domain structures in Sb-doped GeTe,[102] which are coherent with the large density of planar defects predicted from our XRD results (based on the anisotropic peak broadening and peak shifts of some particular reflections) on Zr-Sb codoped GeTe. The commingled effects of band structure modulations to markedly improve the thermopower and the suppression of both electronic and lattice contribution to stupendously reduce the thermal conductivity in Zr-Sb codoped $Ge_{0.88}Zr_{0.005}Sb_{0.10}Te$ sample have enabled it to manifest a high zT_{max} ~1.8 at 723 K. This zT value is on par with or better than some of best reported GeTe materials that were reportedly codoped with Bi-Sb,[47] Mn-Bi,[82] Mn-Sb,[63] Ga-Sb,[35] Ti-Bi,[57] *etc*. However, it must be mentioned that the recent improvisations (especially the symmetry-breaking approach) have reportedly yielded $zT \geq 2$ in some of the codoped GeTe compounds.[48,77,81,103,107]

According to the DFT calculations, doping of Sb reportedly decreases the energy of mixing in GeTe (*i.e.*, the formation energy of the alloy),[35,47,81,103] and this provides scope for increased solubility of Zr in such Sb-codoped GeTe compositions. This renders further avenues for future work to explore more and optimize the Zr-content in these Zr-Sb codoped GeTe compositions to reach $zT > 2$.

4. Conclusion

To summarize, combined experimental and theoretical methods allowed us to extensively screen a family of transition and rare-earth elements as potential dopants for GeTe compounds for thermoelectric application. Each of their effects is summed up as follows,

(1) The presence of the cubic GeTe secondary phase affected the thermal conductivity in Nb-doped GeTe.

(2) Ru-doping produced several intruder states in the band gap of GeTe and profoundly affected the electrical transport properties. The presence of the secondary GeTe cubic phase also severely affected the thermal conductivity. The combined detrimental effect to both electrical and thermal transport properties with Ru-doping resulted in the least TE performance (least zT) among the transition and rare-earth materials that are reported in this work.

(3) Mo-doping produced intruder states in the band gap of GeTe and also exhibited some magnetic character. Overall, PF was not affected much when compared to pristine GeTe, however, κ was increased.

(4) Pr-doping, though, did not influence much the electrical transport properties, adversely affected κ due to the presence of a large proportion of secondary GeTe cubic phase.

(5) V-doping produced flat and localized intruder states within the gap, and also distorted the density of states (induced resonance states adjacent to the Fermi level). These band modifications coupled with some magnetic character – all of which are known to suppress the charge carrier mobility – resulted in high resistivity and hence low PF. Unit cell volume also shrank with the substitution of V for Ge.

(6) Y-doping did not change much the electronic band structure of GeTe, and hence comparable PF are measured. But the κ was reduced, thus resulting in a marginal improvement in zT.

(7) Hf-doping tends to marginally decrease the energy separation between the two valence bands, thus slightly boosting PF and overall zT.

(8) La-doping neither changed κ nor the energy separation between the two valence bands, but the band gap was slightly opened up, and PF (hence overall zT) was slightly improved.

(9) Zr-doping did not change κ, but opened up the band gap and decreased the energy separation between the two valence bands, resulting in improvement in PF and overall zT.

(10) Creating Ge-deficiencies (vacancies) and modulating it with Zr-doping resulted in a large density of planar defects (deduced by the super-Lorentzian profile from XRD), leading to a significant reduction in κ and a marked improvement in zT from 0.85 (for pristine GeTe) to 1.3 at 673 K for Ge-deficient Zr-doped GeTe. Moving forward, this novel unconventional method of producing more electrically dormant Ge-vacancies and balancing it with an aliovalent metallic dopant as a strategic route for producing highly efficient GeTe-based TE materials *via* suppression of thermal transport properties without noticeably affecting the electrical transport properties.

(11) Zr-Sb codoping in GeTe resulted in an improved band degeneracy and facilitated the convergence of electronic band valleys (thus improving the Seebeck) with the tuning of the crystal field effect (reduction in c/a ratio) and suppressed the thermal transport, thus resulting in an exceptionally high zT ~ 1.8 at 723 K, comparable with some of the best reported high-performance codoped GeTe materials.

Acknowledgment

B.S and S.L.T acknowledge the JSPS postdoctoral fellowships P19720 and PE19749, respectively. Support from JSPS KAKENHI 19F19720, JP16H06441 and JST-Mirai JPMJMI19A1 project grants are also gratefully acknowledged.

References

1 L. E. Bell, *Science*, 2008, **321**, 1457–1461.
2 T. Mori and S. Priya, *MRS Bull.*, 2018, **43**, 176–180.

3 I. Petsagkourakis, K. Tybrandt, X. Crispin, I. Ohkubo, N. Satoh and T. Mori, *Sci. Technol. Adv. Mater.*, 2018, **19**, 836–862.

4 B. Srinivasan, Novel chalcogenide based glasses, ceramics and polycrystalline materials for thermoelectric application. PhD Thesis, *Université Rennes 1*, France, 2018. ⟨NNT : 2018REN1S036⟩, ⟨tel-01974992⟩

5 J. R. Sootsman, H. Kong, C. Uher, J. J. D'Angelo, C.-I. Wu, T. P. Hogan, T. Caillat and M. G. Kanatzidis, *Angew. Chem. Int. Ed.*, 2008, **47**, 8618–8622.

6 X. Su, P. Wei, H. Li, W. Liu, Y. Yan, P. Li, C. Su, C. Xie, W. Zhao, P. Zhai, Q. Zhang, X. Tang and C. Uher, *Adv. Mater.*, 2017, **29**, 1602013.

7 Y. Zheng, Q. Zhang, X. Su, H. Xie, S. Shu, T. Chen, G. Tan, Y. Yan, X. Tang, C. Uher and G. J. Snyder, *Adv. Energy Mater.*, 2015, **5**, 1401391.

8 T. Mori, *Small*, 2017, **13**, 1702013.

9 A. U. Khan, K. Kobayashi, D.-M. Tang, Y. Yamauchi, K. Hasegawa, M. Mitome, Y. Xue, B. Jiang, K. Tsuchiya, D. Golberg, Y. Bando and T. Mori, *Nano Energy*, 2017, **31**, 152–159.

10 B. C. Sales, D. Mandrus and R. K. Williams, *Science*, 1996, **272**, 1325–1328.

11 D. T. Morelli, V. Jovovic and J. P. Heremans, *Phys. Rev. Lett.*, 2008, **101**, 035901.

12 M. K. Jana and K. Biswas, *ACS Energy Lett.*, 2018, **3**, 1315–1324.

13 M. Samanta, K. Pal, P. Pal, U. V. Waghmare and K. Biswas, *J. Am. Chem. Soc.*, 2018, **140**, 5866–5872.

14 A. Banik, U. S. Shenoy, S. Anand, U. V. Waghmare and K. Biswas, *Chem. Mater.*, 2015, **27**, 581–587.

15 Y. Pei, X. Shi, A. LaLonde, H. Wang, L. Chen and G. J. Snyder, *Nature*, 2011, **473**, 66–69.

16 Q. Zhang, B. Liao, Y. Lan, K. Lukas, W. Liu, K. Esfarjani, C. Opeil, D. Broido, G. Chen and Z. Ren, *Proc. Natl. Acad. Sci. U. S. A.*, 2013, **110**, 13261–13266.

17 L. D. Hicks and M. S. Dresselhaus, *Phys. Rev. B*, 1993, **47**, 12727–12731.

18 S. Lin, W. Li, Z. Chen, J. Shen, B. Ge and Y. Pei, *Nat. Commun.*, 2016, **7**, 10287.

19 J. M. O. Zide, D. Vashaee, Z. X. Bian, G. Zeng, J. E. Bowers, A. Shakouri and A. C. Gossard, *Phys. Rev. B*, 2006, **74**, 205335.

20 A. Pakdel, Q. Guo, V. Nicolosi and T. Mori, *J. Mater. Chem. A*, 2018, **6**, 21341–21349.

21 M. S. Dresselhaus, G. Chen, M. Y. Tang, R. G. Yang, H. Lee, D. Z. Wang, Z. F. Ren, J.-P. Fleurial and P. Gogna, *Adv. Mater.*, 2007, **19**, 1043–1053.

22 Y. Pei, A. D. LaLonde, H. Wang and G. J. Snyder, *Energy Environ. Sci.*, 2012, **5**, 7963–7969.

23 H. Wang, Y. Pei, A. D. LaLonde and G. J. Snyder, *Proc. Natl. Acad. Sci.*, 2012, **109**, 9705–9709.

24 J. R. Szczech, J. M. Higgins and S. Jin, *J Mater Chem*, 2011, **21**, 4037–4055.

25 J. R. Sootsman, D. Y. Chung and M. G. Kanatzidis, *Angew. Chem. Int. Ed.*, 2009, **48**, 8616–8639.

26 R. Ang, A. U. Khan, N. Tsujii, K. Takai, R. Nakamura and T. Mori, *Angew. Chem. Int. Ed.*, 2015, **54**, 12909–12913.

27 J.-B. Vaney, S. Aminorroaya Yamini, H. Takaki, K. Kobayashi, N. Kobayashi and T. Mori, *Mater. Today Phys.*, 2019, **9**, 100090.

28 K. Vandaele, S. J. Watzman, B. Flebus, A. Prakash, Y. Zheng, S. R. Boona and J. P. Heremans, *Mater. Today Phys.*, 2017, **1**, 39–49.

29 F. Ahmed, N. Tsujii and T. Mori, *J. Mater. Chem. A*, 2017, **5**, 7545–7554.

30 B. Srinivasan, S. Cui, C. Prestipino, A. Gellé, C. Boussard-Pledel, S. Ababou-Girard, A. Trapananti, B. Bureau and S. Di Matteo, *J. Phys. Chem. C*, 2017, **121**, 14045–14050.

31 P. Lucas, C. Conseil, Z. Yang, Q. Hao, S. Cui, C. Boussard-Pledel, B. Bureau, F. Gascoin, C. Caillaud, O. Gulbiten, T. Guizouarn, P. Baruah, Q. Li and J. Lucas, *J. Mater. Chem. A*, 2013, **1**, 8917–8925.

32 B. Srinivasan, C. Boussard-Pledel, V. Dorcet, M. Samanta, K. Biswas, R. Lefèvre, F. Gascoin, F. Cheviré, S. Tricot, M. Reece and B. Bureau, *Materials*, 2017, **10**, 328.

33 A. P. Gonçalves, E. B. Lopes, G. Delaizir, J. B. Vaney, B. Lenoir, A. Piarristeguy, A. Pradel, J. Monnier, P. Ochin and C. Godart, *J. Solid State Chem.*, 2012, **193**, 26–30.

34 T. Zhang, Z. Wang, B. Srinivasan, Z. Wang, J. Zhang, K. Li, C. Boussard-Pledel, J. Troles, B. Bureau and L. Wei, *ACS Appl. Mater. Interfaces*, 2019, **11**, 2441–2447.

35 B. Srinivasan, A. Gellé, F. Gucci, C. Boussard-Pledel, B. Fontaine, R. Gautier, J.-F. Halet, M. J. Reece and B. Bureau, *Inorg. Chem. Front.*, 2019, **6**, 63–73.

36 B. Srinivasan, B. Fontaine, F. Gucci, V. Dorcet, T. G. Saunders, M. Yu, F. Cheviré, C. Boussard-Pledel, J.-F. Halet, R. Gautier, M. J. Reece and B. Bureau, *Inorg. Chem.*, 2018, **57**, 12976–12986.
37 F. Gucci, T. G. Saunders, B. Srinivasan, F. Cheviré, D. A. Ferluccio, J.-W. G. Bos and M. J. Reece, *J. Alloys Compd.*, 2020, **837**, 155058.
38 D. Bilc, S. D. Mahanti, E. Quarez, K.-F. Hsu, R. Pcionek and M. G. Kanatzidis, *Phys. Rev. Lett.*, 2004, **93**, 146403.
39 Q. Zhang, F. Cao, W. Liu, K. Lukas, B. Yu, S. Chen, C. Opeil, D. Broido, G. Chen and Z. Ren, *J. Am. Chem. Soc.*, 2012, **134**, 10031–10038.
40 R. Al Rahal Al Orabi, N. A. Mecholsky, J. Hwang, W. Kim, J.-S. Rhyee, D. Wee and M. Fornari, *Chem. Mater.*, 2016, **28**, 376–384.
41 A. Banik, U. S. Shenoy, S. Saha, U. V. Waghmare and K. Biswas, *J. Am. Chem. Soc.*, 2016, **138**, 13068–13075.
42 L. Wang, X. Tan, G. Liu, J. Xu, H. Shao, B. Yu, H. Jiang, S. Yue and J. Jiang, *ACS Energy Lett.*, 2017, **2**, 1203–1207.
43 A. Banik, S. Roychowdhury and K. Biswas, *Chem. Commun.*, 2018, **54**, 6573–6590.
44 W. Liu, X. Tan, K. Yin, H. Liu, X. Tang, J. Shi, Q. Zhang and C. Uher, *Phys. Rev. Lett.*, 2012, **108**, 166601.
45 C. Fu, S. Bai, Y. Liu, Y. Tang, L. Chen, X. Zhao and T. Zhu, *Nat. Commun.*, 2015, **6**, 8144.
46 S. Perumal, S. Roychowdhury and K. Biswas, *J. Mater. Chem. C*, 2016, **4**, 7520–7536.
47 S. Perumal, P. Bellare, U. S. Shenoy, U. V. Waghmare and K. Biswas, *Chem. Mater.*, 2017, **29**, 10426–10435.
48 J. Li, X. Zhang, Z. Chen, S. Lin, W. Li, J. Shen, I. T. Witting, A. Faghaninia, Y. Chen, A. Jain, L. Chen, G. J. Snyder and Y. Pei, *Joule*, 2018, **2**, 976–987.
49 J. Li, X. Zhang, X. Wang, Z. Bu, L. Zheng, B. Zhou, F. Xiong, Y. Chen and Y. Pei, *J. Am. Chem. Soc.*, 2018, **140**, 16190–16197.
50 J. Dong, F.-H. Sun, H. Tang, J. Pei, H.-L. Zhuang, H.-H. Hu, B.-P. Zhang, Y. Pan and J.-F. Li, *Energy Environ. Sci.*, 2019, **12**, 1396–1403.
51 K. S. Bayikadi, R. Sankar, C. T. Wu, C. Xia, Y. Chen, L.-C. Chen, K.-H. Chen and F.-C. Chou, *J. Mater. Chem. A*, 2019, **7**, 15181–15189.
52 M. Hong, J. Zou and Z.-G. Chen, *Adv. Mater.*, 2019, **31**, 1807071.
53 Y. Gelbstein and J. Davidow, *Phys. Chem. Chem. Phys.*, 2014, **16**, 20120–20126.
54 S. Perumal, S. Roychowdhury and K. Biswas, *Inorg. Chem. Front.*, 2016, **3**, 125–132.
55 L. Wu, X. Li, S. Wang, T. Zhang, J. Yang, W. Zhang, L. Chen and J. Yang, *NPG Asia Mater.*, 2017, **9**, e343.
56 J. Shuai, Y. Sun, X. Tan and T. Mori, *Small*, 2020, **16**, 1906921.
57 J. Shuai, X. J. Tan, Q. Guo, J. T. Xu, A. Gellé, R. Gautier, J.-F. Halet, F. Failamani, J. Jiang and T. Mori, *Mater. Today Phys.*, 2019, **9**, 100094.
58 B. Srinivasan, A. Gellé, J.-F. Halet, C. Boussard-Pledel and B. Bureau, *Materials*, 2018, **11**, 2237.
59 L. Yang, J. Q. Li, R. Chen, Y. Li, F. S. Liu and W. Q. Ao, *J. Electron. Mater.*, 2016, **45**, 5533–5539.
60 S. Perumal, S. Roychowdhury, D. S. Negi, R. Datta and K. Biswas, *Chem. Mater.*, 2015, **27**, 7171–7178.
61 E. Nshimyimana, X. Su, H. Xie, W. Liu, R. Deng, T. Luo, Y. Yan and X. Tang, *Sci. Bull.*, 2018, **63**, 717–725.
62 B. Srinivasan, R. Gautier, F. Gucci, B. Fontaine, J.-F. Halet, F. Cheviré, C. Boussard-Pledel, M. J. Reece and B. Bureau, *J. Phys. Chem. C*, 2018, **122**, 227–235.
63 Z. Zheng, X. Su, R. Deng, C. Stoumpos, H. Xie, W. Liu, Y. Yan, S. Hao, C. Uher, C. Wolverton, M. G. Kanatzidis and X. Tang, *J. Am. Chem. Soc.*, 2018, **140**, 2673–2686.
64 J. K. Lee, M. W. Oh, B. S. Kim, B. K. Min, H. W. Lee and S. D. Park, *Electron. Mater. Lett.*, 2014, **10**, 813–817.
65 B. Srinivasan, D. Berthebaud and T. Mori, *Energies*, 2020, **13**, 643.
66 S. H. Yang, T. J. Zhu, T. Sun, J. He, S. N. Zhang and X. B. Zhao, *Nanotechnology*, 2008, **19**, 245707.

67 T. Schröder, T. Rosenthal, N. Giesbrecht, S. Maier, E.-W. Scheidt, W. Scherer, G. J. Snyder, W. Schnick and O. Oeckler, *J. Mater. Chem. A*, 2014, **2**, 6384–6395.

68 T. Schröder, S. Schwarzmüller, C. Stiewe, J. de Boor, M. Hölzel and O. Oeckler, *Inorg. Chem.*, 2013, **52**, 11288–11294.

69 F. Fahrnbauer, D. Souchay, G. Wagner and O. Oeckler, *J. Am. Chem. Soc.*, 2015, **137**, 12633–12638.

70 S. Chen, H. Bai, J. Li, W. Pan, X. Jiang, Z. Li, Z. Chen, Y. Yan, X. Su, J. Wu, C. Uher and X. Tang, *ACS Appl. Mater. Interfaces*, 2020, **12**, 19664–19673.

71 M. Samanta, S. Roychowdhury, J. Ghatak, S. Perumal and K. Biswas, *Chem. – Eur. J.*, n/a-n/a.

72 D. Wu, L.-D. Zhao, S. Hao, Q. Jiang, F. Zheng, J. W. Doak, H. Wu, H. Chi, Y. Gelbstein, C. Uher, C. Wolverton, M. Kanatzidis and J. He, *J. Am. Chem. Soc.*, 2014, **136**, 11412–11419.

73 J. Li, X. Zhang, S. Lin, Z. Chen and Y. Pei, *Chem. Mater.*, 2017, **29**, 605–611.

74 Y. Rosenberg, Y. Gelbstein and M. P. Dariel, *J. Alloys Compd.*, 2012, **526**, 31–38.

75 M. Samanta and K. Biswas, *J. Am. Chem. Soc.*, 2017, **139**, 9382–9391.

76 B. Srinivasan, C. Boussard-Pledel and B. Bureau, *Mater. Lett.*, 2018, **230**, 191–194.

77 S. Perumal, M. Samanta, T. Ghosh, U. S. Shenoy, A. K. Bohra, S. Bhattacharya, A. Singh, U. V. Waghmare and K. Biswas, *Joule*, 2019, **3**, 2565–2580.

78 E. M. Levin, S. L. Bud'ko and K. Schmidt-Rohr, *Adv. Funct. Mater.*, 2012, **22**, 2766–2774.

79 M. Hong, Y. Wang, W. Liu, S. Matsumura, H. Wang, J. Zou and Z.-G. Chen, *Adv. Energy Mater.*, 2018, **8**, 1801837.

80 E. M. Levin, B. A. Cook, J. L. Harringa, S. L. Bud'ko, R. Venkatasubramanian and K. Schmidt-Rohr, *Adv. Funct. Mater.*, 2011, **21**, 441–447.

81 M. Hong, Y. Wang, T. Feng, Q. Sun, S. Xu, S. Matsumura, S. T. Pantelides, J. Zou and Z.-G. Chen, *J. Am. Chem. Soc.*, 2019, **141**, 1742–1748.

82 Z. Liu, J. Sun, J. Mao, H. Zhu, W. Ren, J. Zhou, Z. Wang, D. J. Singh, J. Sui, C.-W. Chu and Z. Ren, *Proc. Natl. Acad. Sci.*, 2018, **115**, 5332–5337.

83 J. R. Gandhi, R. Nehru, S.-M. Chen, R. Sankar, K. S. Bayikadi, P. Sureshkumar, K.-H. Chen and L.-C. Chen, *CrystEngComm*, 2018, **20**, 6449–6457.

84 J. Rodríguez-Carvajal, *Phys. B Condens. Matter*, 1993, **192**, 55–69.

85 T. Roisnel and J. Rodríguez-Carvajal, in *Materials Science Forum*, 2001, vol. 378–381, pp. 118–123.

86 A. L. Bail, *Powder Diffr.*, 2005, **20**, 316–326.

87 P. Thompson, D. E. Cox and J. B. Hastings, *J. Appl. Crystallogr.*, 1987, **20**, 79–83.

88 J.-F. Bérar and P. Lelann, *J. Appl. Crystallogr.*, 1991, **24**, 1–5.

89 H.-S. Kim, Z. M. Gibbs, Y. Tang, H. Wang and G. J. Snyder, *APL Mater.*, 2015, **3**, 041506.

90 J. Simon, G. Guélou, B. Srinivasan, D. Berthebaud, T. Mori and A. Maignan, *J. Alloys Compd.*, 2020, **819**, 152999.

91 G. Kresse and D. Joubert, *Phys. Rev. B*, 1999, **59**, 1758–1775.

92 G. Kresse and J. Furthmüller, *Phys. Rev. B*, 1996, **54**, 11169–11186.

93 J. P. Perdew, K. Burke and M. Ernzerhof, *Phys. Rev. Lett.*, 1996, **77**, 3865–3868.

94 K. Hoang, S. D. Mahanti and M. G. Kanatzidis, *Phys. Rev. B*, 2010, **81**, 115106.

95 S. L. Dudarev, G. A. Botton, S. Y. Savrasov, C. J. Humphreys and A. P. Sutton, *Phys. Rev. B*, 1998, **57**, 1505–1509.

96 M. Musa Saad H.-E., *Mater. Chem. Phys.*, 2018, **204**, 350–360.

97 E. M. Levin, M. F. Besser and R. Hanus, *J. Appl. Phys.*, 2013, **114**, 083713.

98 E. M. Levin, *Phys. Rev. B*, 2016, **93**, 045209.

99 A. H. Edwards, A. C. Pineda, P. A. Schultz, M. G. Martin, A. P. Thompson, H. P. Hjalmarson and C. J. Umrigar, *Phys. Rev. B*, 2006, **73**, 045210.

100 T. Chattopadhyay, J. X. Boucherle and H. G. vonSchnering, *J. Phys. C Solid State Phys.*, 1987, **20**, 1431–1440.

101 Z. Bu, W. Li, J. Li, X. Zhang, J. Mao, Y. Chen and Y. Pei, *Mater. Today Phys.*, 2019, **9**, 100096.

102 H. S. Lee, B.-S. Kim, C.-W. Cho, M.-W. Oh, B.-K. Min, S.-D. Park and H.-W. Lee, *Acta Mater.*, 2015, **91**, 83–90.

103 M. Hong, Z.-G. Chen, L. Yang, Y.-C. Zou, M. S. Dargusch, H. Wang and J. Zou, *Adv. Mater.*, 2018, **30**, 1705942.

104 S. Evangelisti, J. P. Daudey and J. P. Malrieu, *Phys. Rev. A*, 1987, **35**, 4930–4941.

105 C. Angeli, M. Pastore and R. Cimiraglia, *Theor. Chem. Acc.*, 2007, **117**, 743–754.

106 S. Acharya, S. Anwar, T. Mori and A. Soni, *J. Mater. Chem. C*, 2018, **6**, 6489–6493.

107 K. S. Bayikadi, C. T. Wu, L.-C. Chen, K.-H. Chen, F.-C. Chou and R. Sankar, *J. Mater. Chem. A*, 2020, **8**, 5332–5341.

108 B. Srinivasan, F. Gucci, C. Boussard-Pledel, F. Cheviré, M. J. Reece, S. Tricot, L. Calvez and B. Bureau, *J. Alloys Compd.*, 2017, **729**, 198–202.

109 P. F. P. Poudeu, J. D'Angelo, H. Kong, A. Downey, J. L. Short, R. Pcionek, T. P. Hogan, C. Uher and M. G. Kanatzidis, *J. Am. Chem. Soc.*, 2006, **128**, 14347–14355.

110 S. Le Tonquesse, Z. Verastegui, H. Huynh, V. Dorcet, Q. Guo, V. Demange, C. Prestipino, D. Berthebaud, T. Mori and M. Pasturel, *ACS Appl. Energy Mater.*, 2019, **2**, 8525–8534.

111 M. Casas-Cabanas, M. Reynaud, J. Rikarte, P. Horbach and J. Rodríguez-Carvajal, *J. Appl. Crystallogr.*, 2016, **49**, 2259–2269.

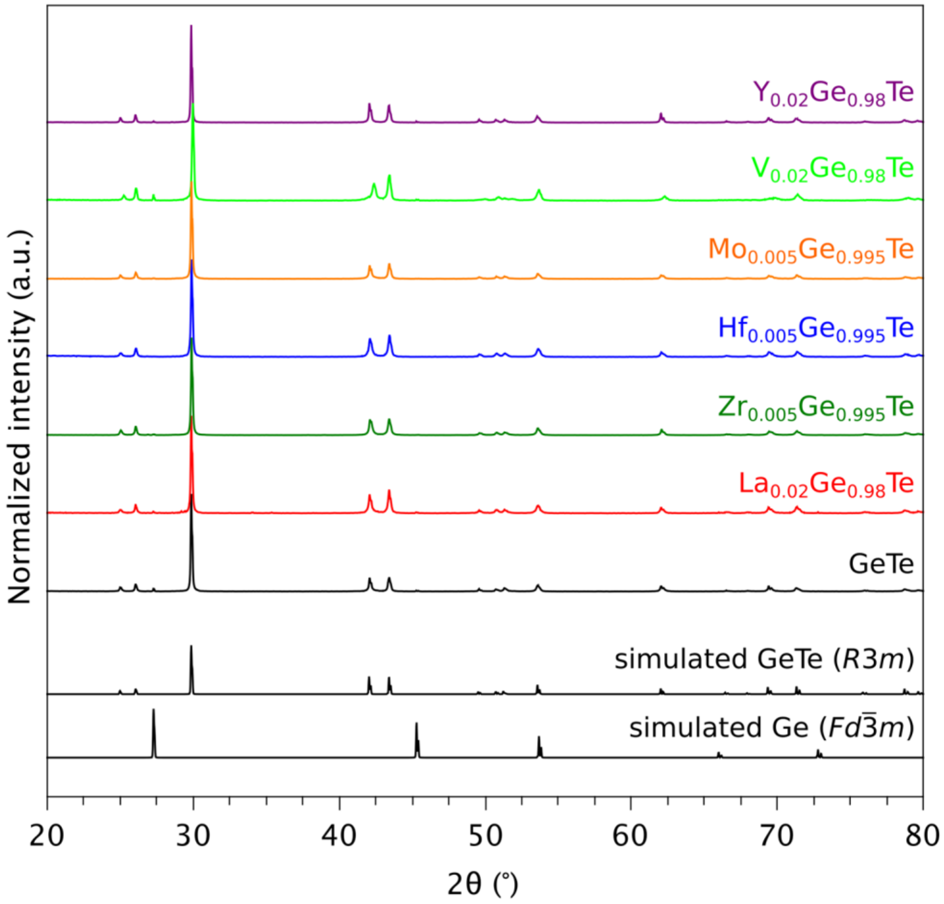

***Figure 1**. Room temperature PXRD patterns for pristine GeTe, $Ge_{0.08}Y_{0.02}Te$, $Ge_{0.995}Hf_{0.005}Te$, $Ge_{0.995}Mo_{0.005}Te$, $Ge_{0.98}V_{0.02}Te$, $Ge_{0.995}Zr_{0.005}Te$, and $Ge_{0.98}La_{0.02}Te$. Simulated patterns for rhombohedral GeTe (main phase) and cubic Ge (impurity) are shown at the bottom of the plots.*

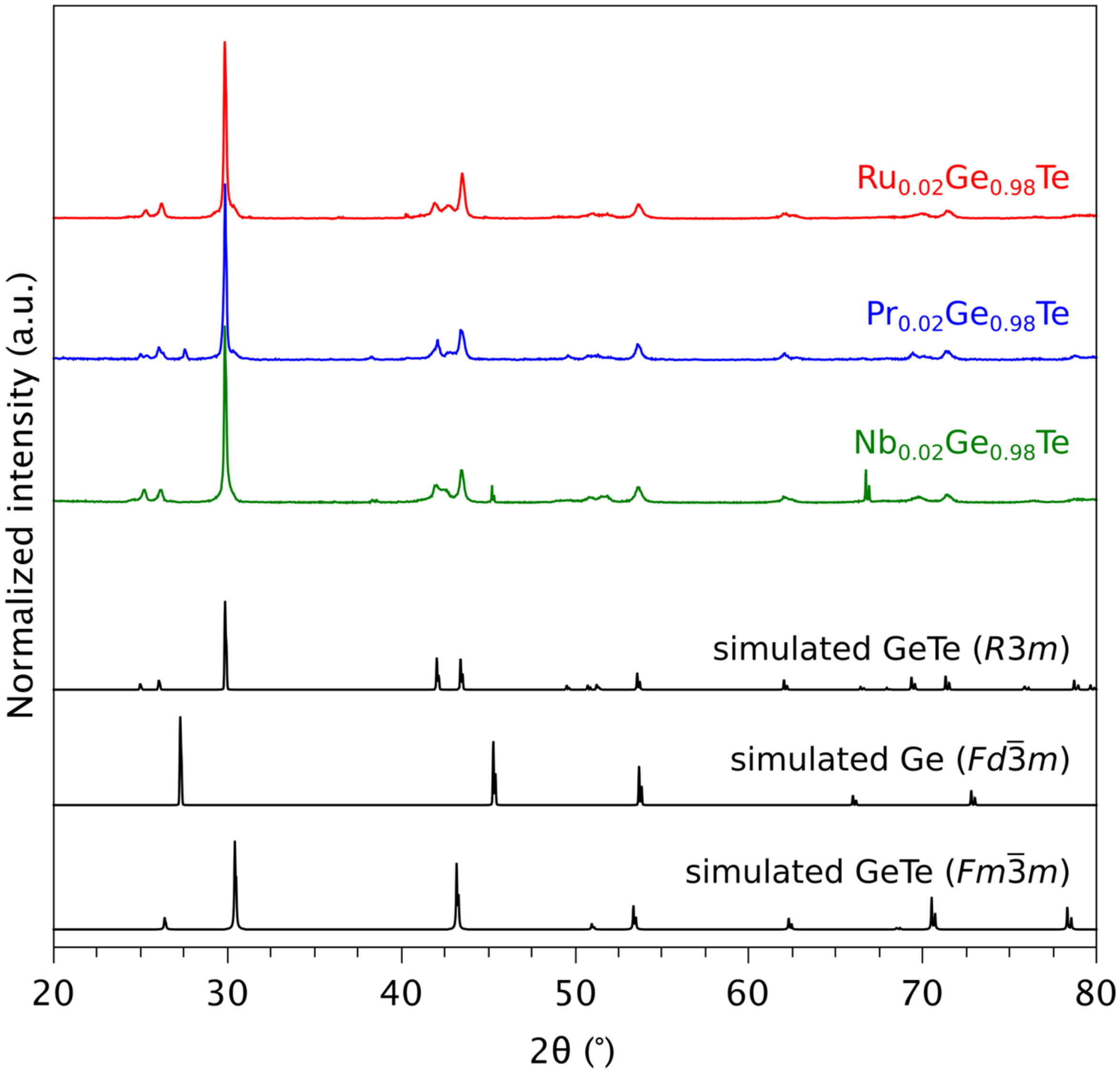

Figure 2. *Room temperature PXRD patterns for* $Ge_{0.98}Ru_{0.02}Te$, $Ge_{0.98}Pr_{0.02}Te$ *and* $Ge_{0.98}Nb_{0.02}Te$. *Simulated patterns for GeTe (cubic and rhombohedral) and Ge are shown at the bottom of the plots. The additional 2θ peaks around 66º for Nb-GeTe came from the sample holder (insufficient powder during XRD sample preparation).*

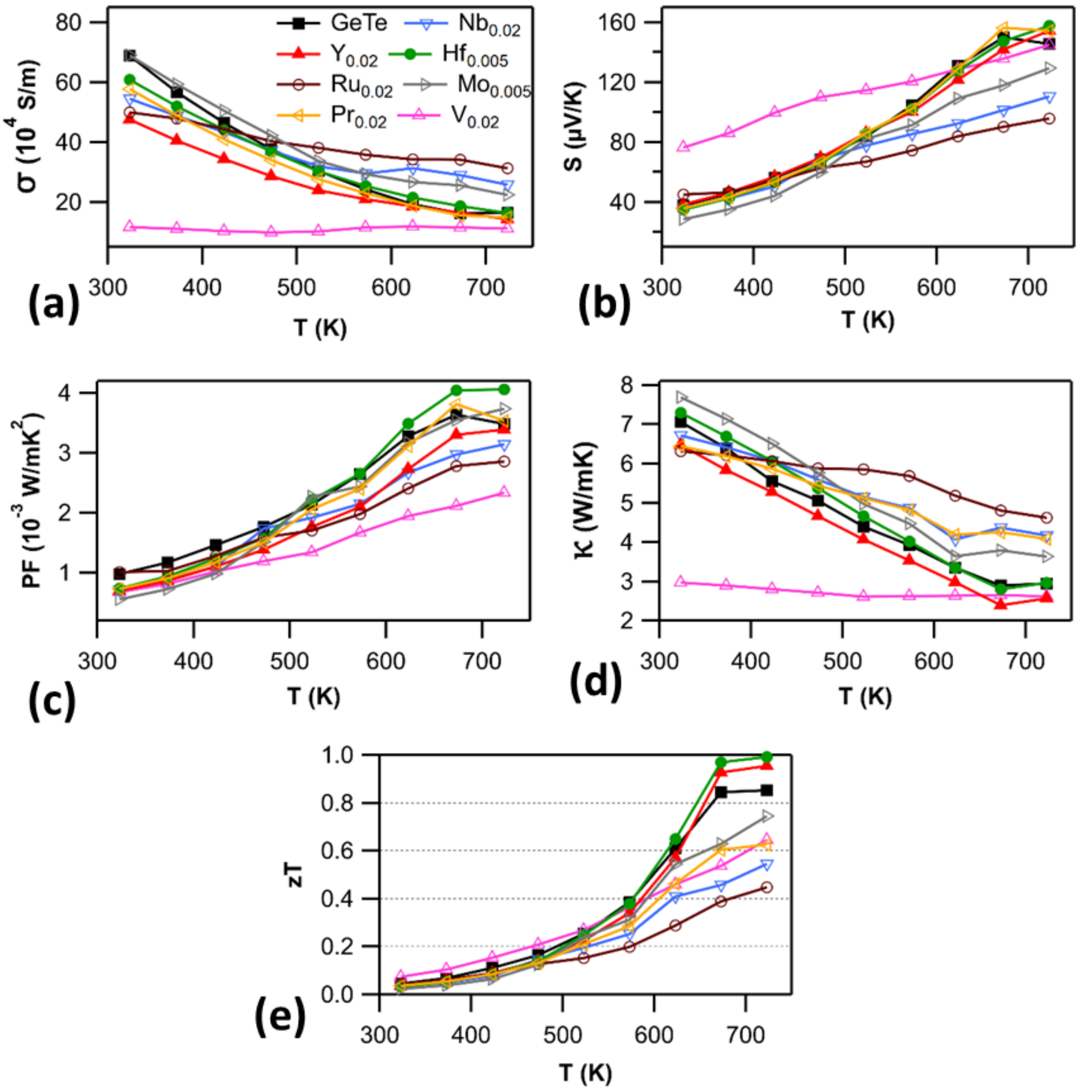

Figure 3. *Temperature-dependent (a) electrical conductivity (σ), (b) Seebeck coefficient (S), (c) power factor (PF = $S^2\sigma$), (d) total thermal conductivity (κ), and (e) figure of merit (zT) for* $Ge_{1-x}M_xTe$ *(x = 0.00, 0.02, 0.005; M = Nb, Y, Hf, Ru, Mo, Pr, and V) compounds.*

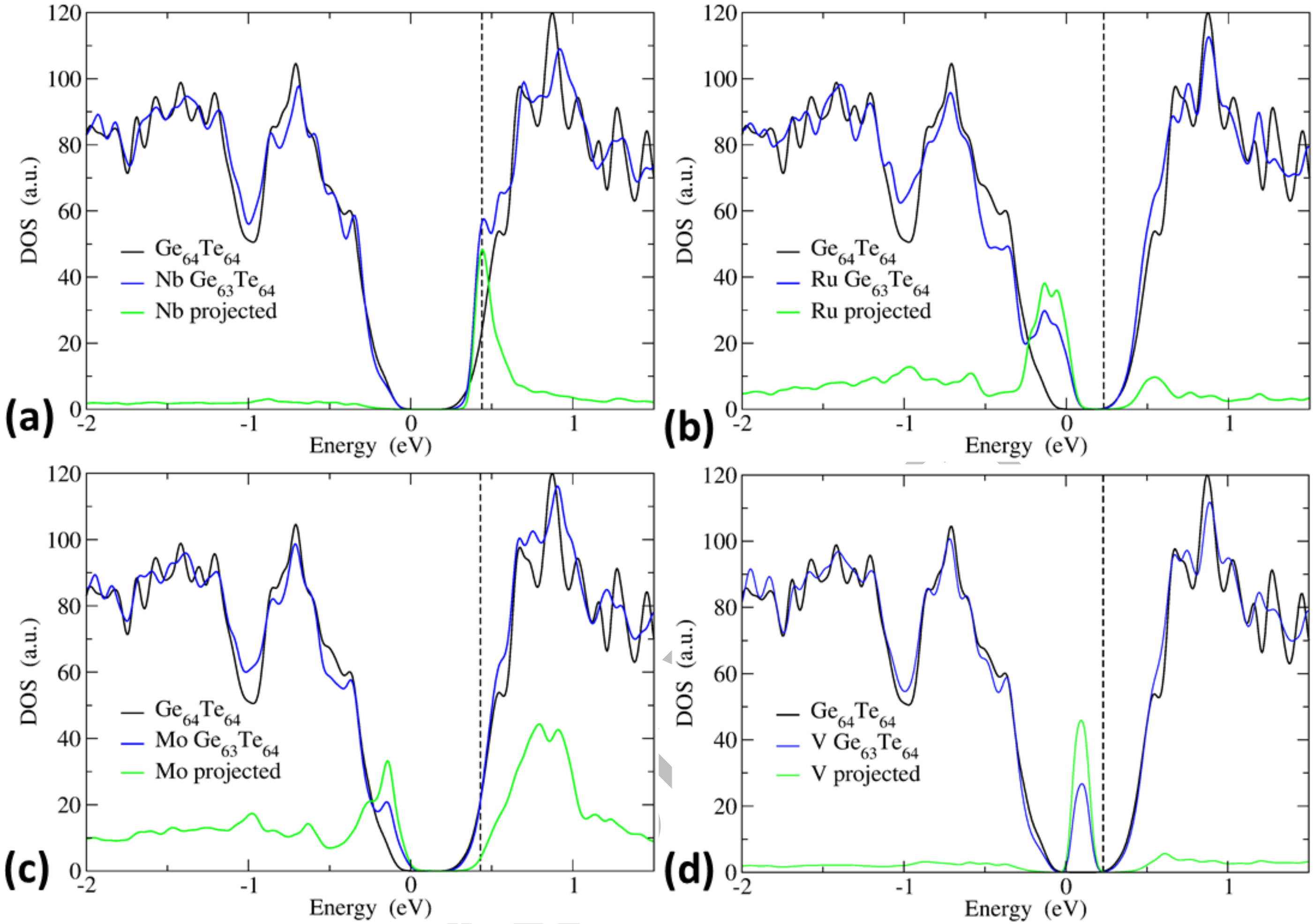

Figure 4. *Calculated DOS for (a) NbGe$_{63}$Te$_{64}$, (b) RuGe$_{63}$Te$_{64}$, (c) MoGe$_{63}$Te$_{64}$, and (d) VGe$_{63}$Te$_{64}$ cubic models. The DOS of each model is compared with that of the pristine c-GeTe (c-Ge$_{64}$Te$_{64}$). The Fermi level (E$_F$) of pristine GeTe is set arbitrarily at 0 eV. The dashed line represents the shifted E$_F$ for the doped compositions. Additional Gaussian smearing of 25 meV was applied and the projected DOS (for dopants) were magnified for better readability of the curves.*

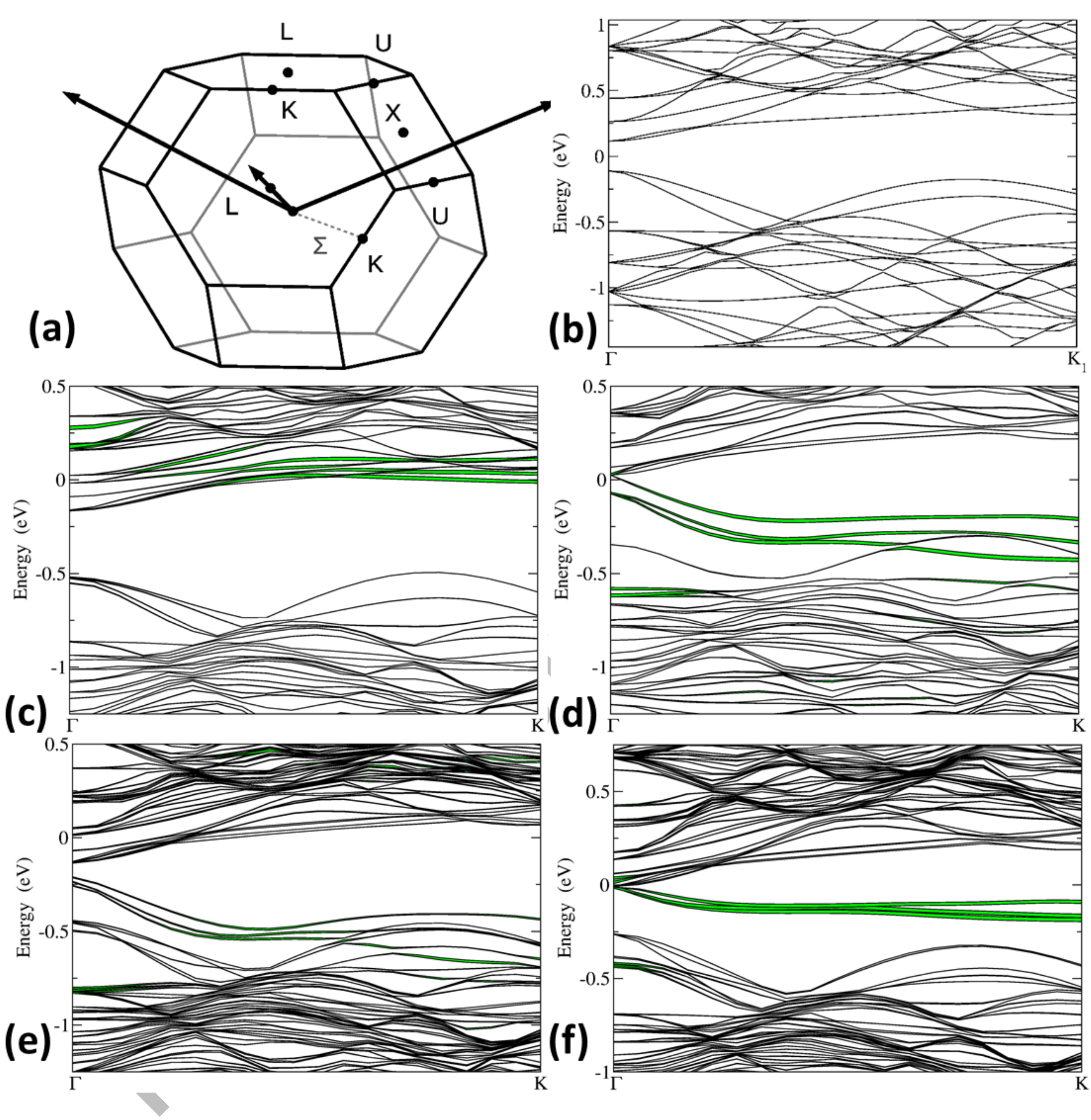

Figure 5. *(a) Brillouin zone of c-GeTe. Band structures of cubic models using a 4 × 4 × 4 supercell showing band folding in the Γ→ K (Σ) direction for (b) pristine c-Ge$_{64}$Te$_{64}$, (c) NbGe$_{63}$Te$_{64}$, (d) RuGe$_{63}$Te$_{64}$, (e) MoGe$_{63}$Te$_{64}$, and (f) VGe$_{63}$Te$_{64}$. The dopant (M = Nb, Ru, Mo, and V) projections are highlighted in green. The line thickness is proportional to the projection of the wave function on the orbitals (in green) of the respective dopants (M = Nb, Ru, Mo, and V).*

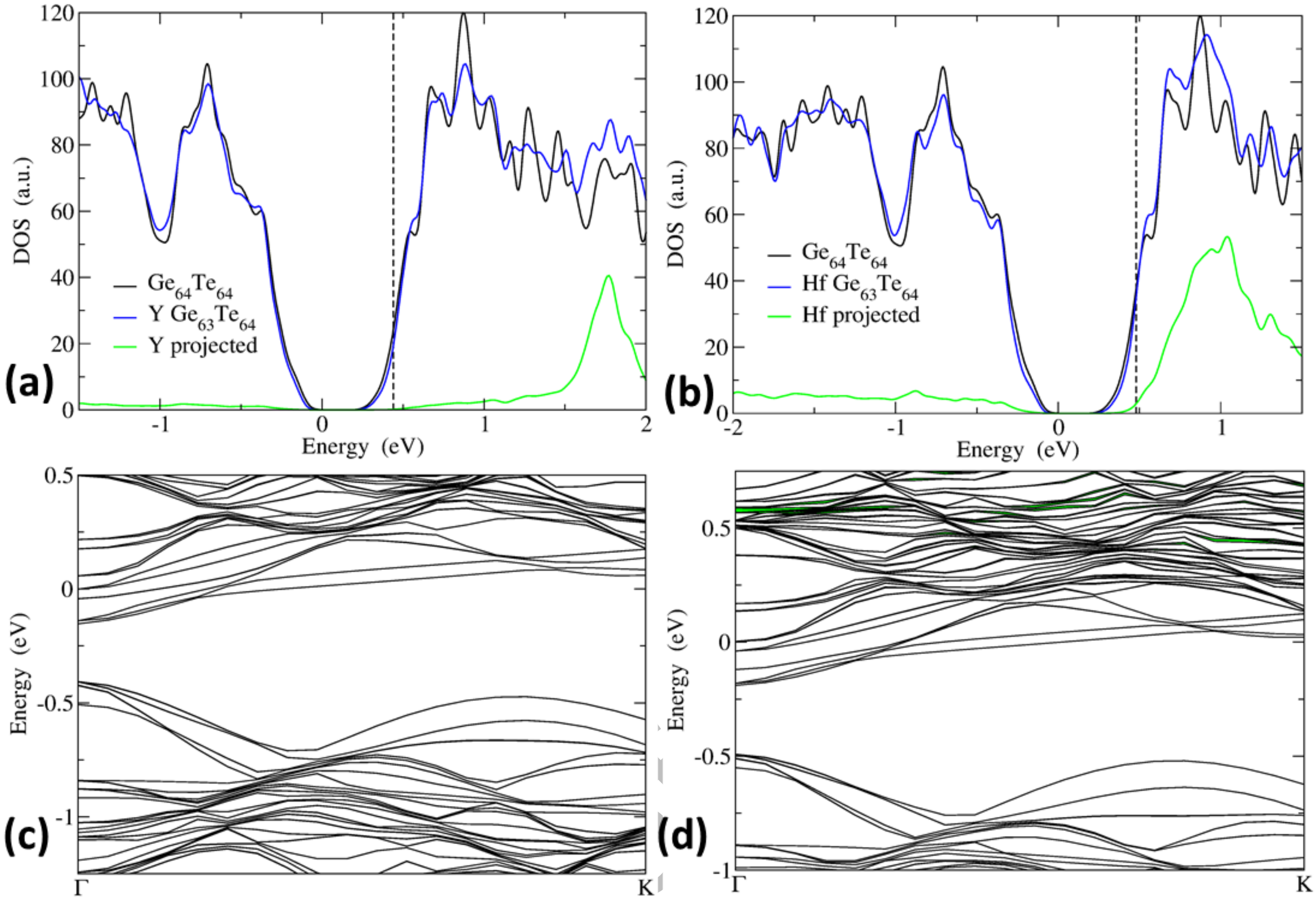

Figure 6. *First-principles computed DOS for (a) $YGe_{63}Te_{64}$ and (b) $HfGe_{63}Te_{64}$, and computed band structures for (c) $YGe_{63}Te_{64}$ and (d) $HfGe_{63}Te_{64}$ cubic models. Additional figure captions (regarding E_F, additional Gaussian smearing, and projection of the wave function) given in Figures 4 and 5, apply also here.*

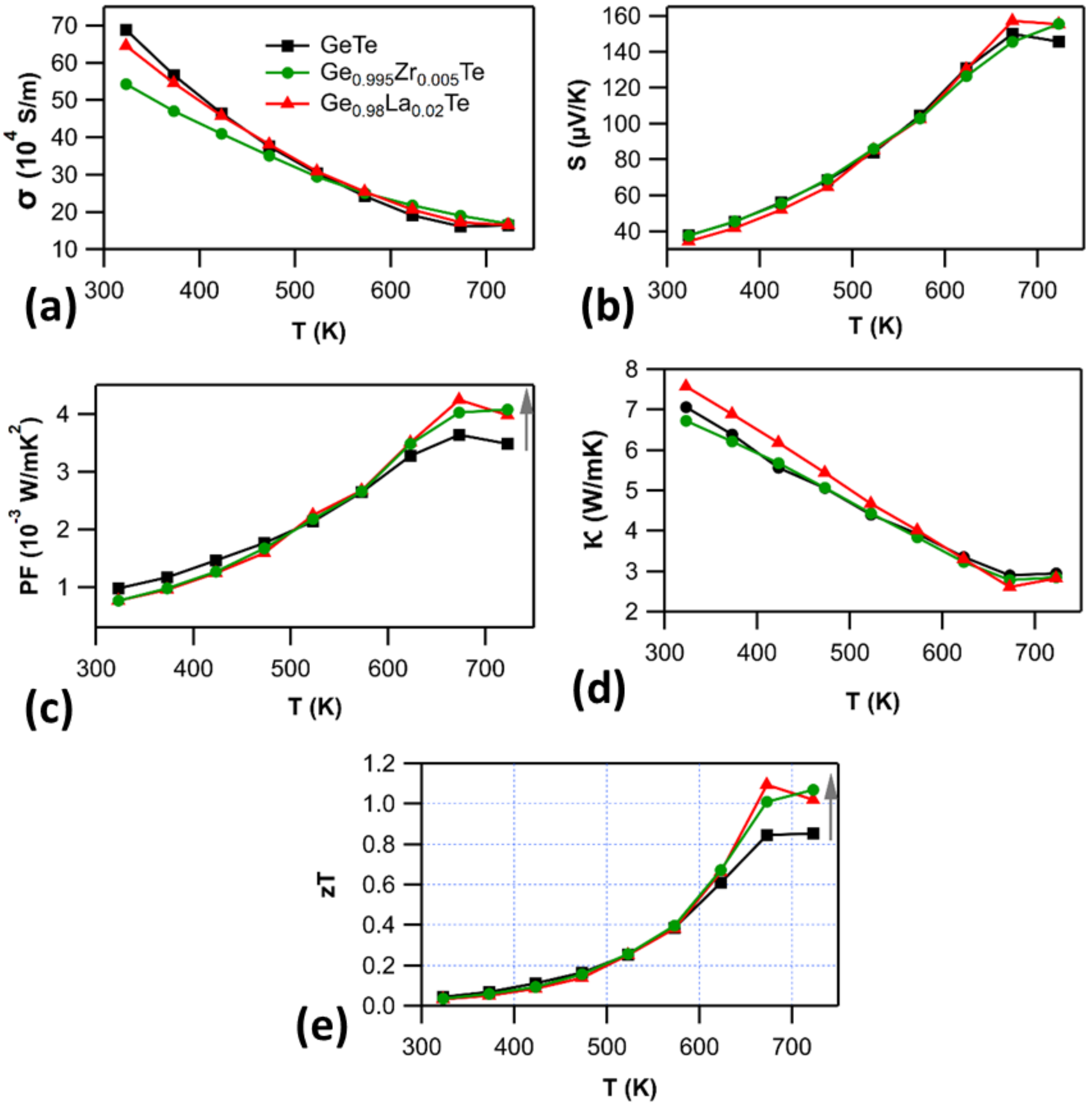

Figure 7. *Temperature-dependent (a) electrical conductivity (σ), (b) Seebeck coefficient (S), (c) power factor (PF = $S^2\sigma$), (d) total thermal conductivity (κ), (e) figure of merit (zT) for* $Ge_{0.995}Zr_{0.005}Te$ *and* $Ge_{0.98}La_{0.02}Te$ *compounds.*

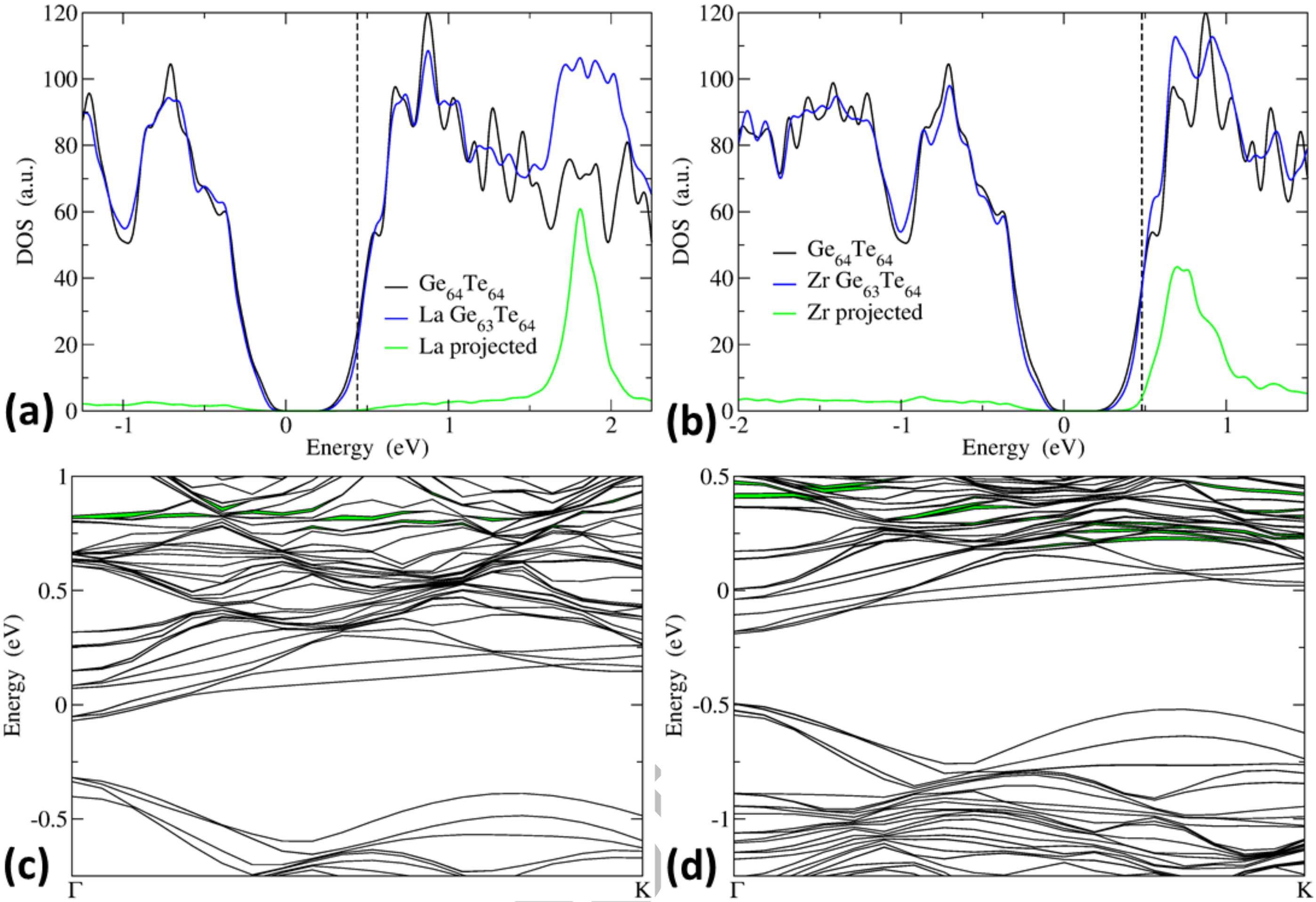

__Figure 8.__ First-principles computed DOS for (a) $LaGe_{63}Te_{64}$ and (b) $ZrGe_{63}Te_{64}$, and computed band structures for (c) $LaGe_{63}Te_{64}$ and (d) $ZrGe_{63}Te_{64}$ cubic models. Additional figure captions (regarding E_F, additional Gaussian smearing, and projection of the wave function) given in Figures 4 and 5, apply also here.

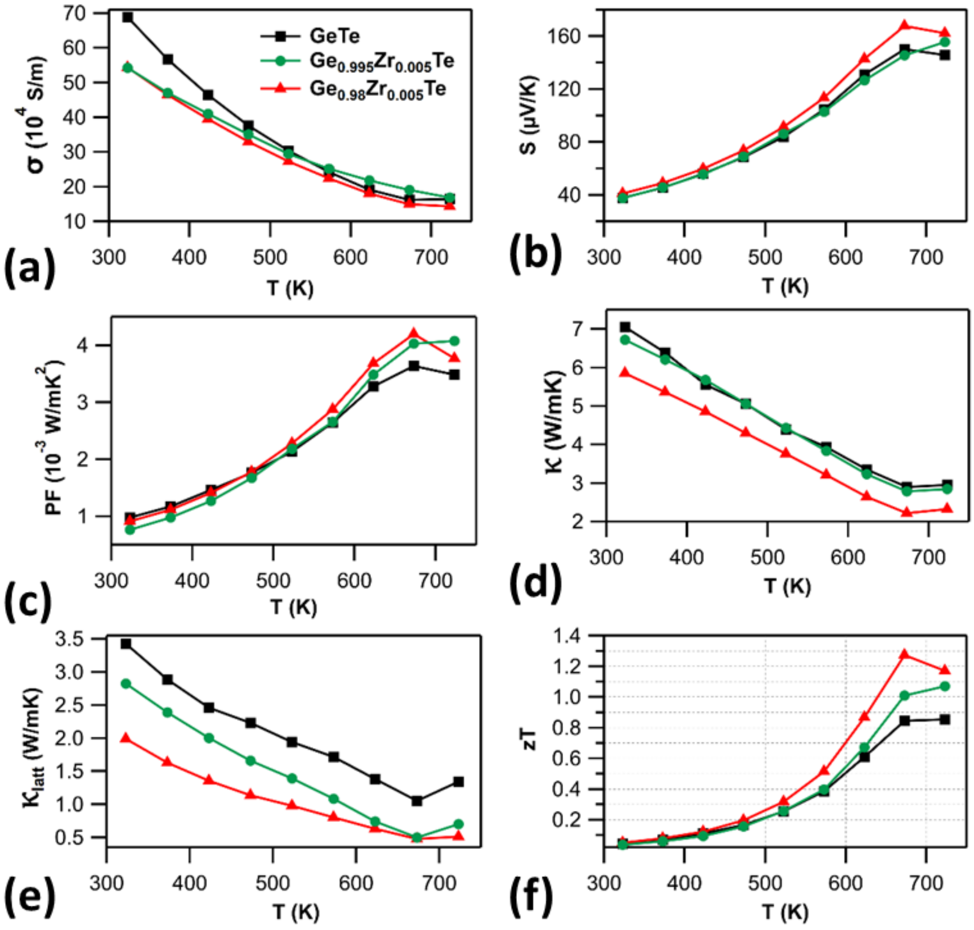

Figure 9. *Temperature-dependent (a) electrical conductivity (σ), (b) Seebeck coefficient (S), (c) power factor (PF = $S^2\sigma$), (d) total thermal conductivity (κ), (e) lattice thermal conductivity (κ_{latt}), and (f) figure of merit (zT) for Ge-deficient $Ge_{0.98}Zr_{0.005}Te$ in comparison with stochiometric $Ge_{0.995}Zr_{0.005}Te$ and pristine GeTe. The Ge deficient $Ge_{0.98}Zr_{0.005}Te$ compound is shown exhibiting superior a zT_{max} ~1.3 at 673 K.*

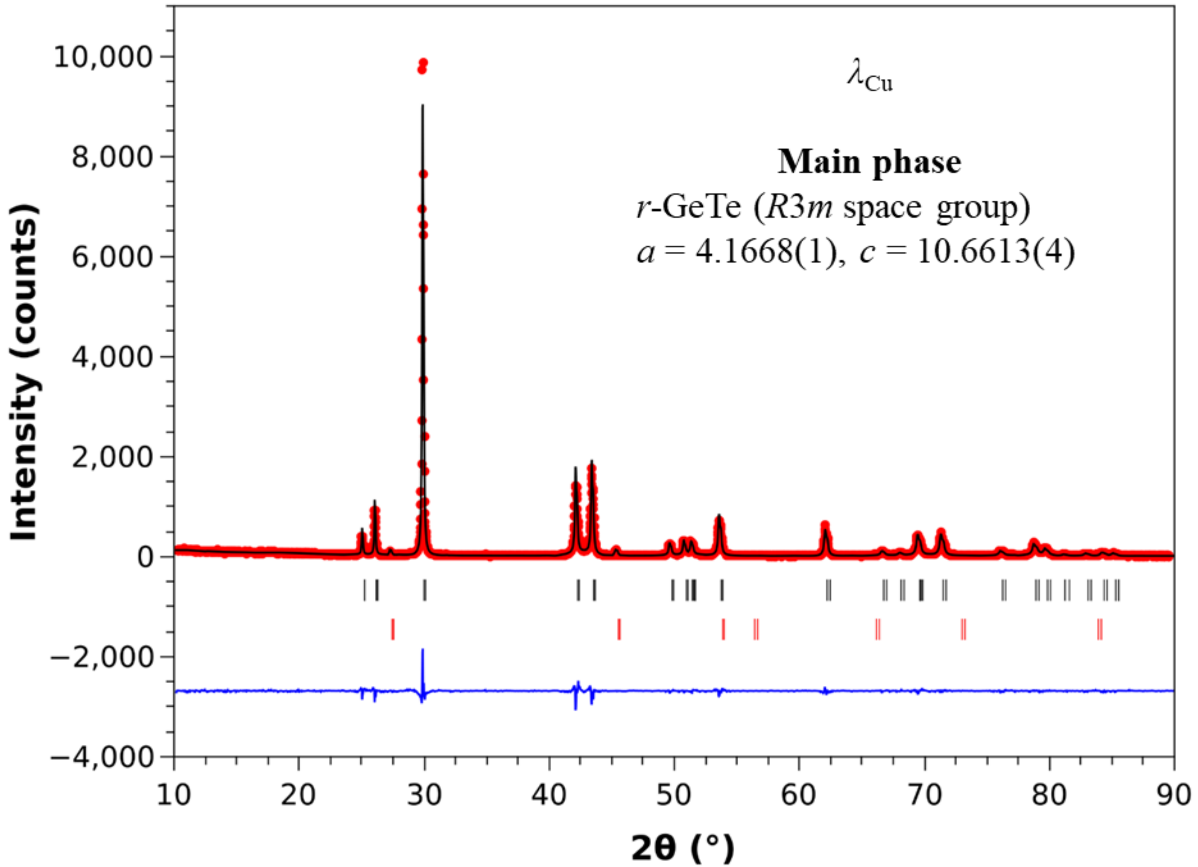

Figure 10. *Le Bail refined room temperature XRD pattern of* $Ge_{0.98}Zr_{0.005}Te$. *The experimental pattern is plotted in red (symbol), the calculated pattern in black (line), and the difference in blue (line). The vertical ticks indicate the Bragg positions of rhombohedral GeTe phase (black) and secondary cubic Ge (red) phase.*

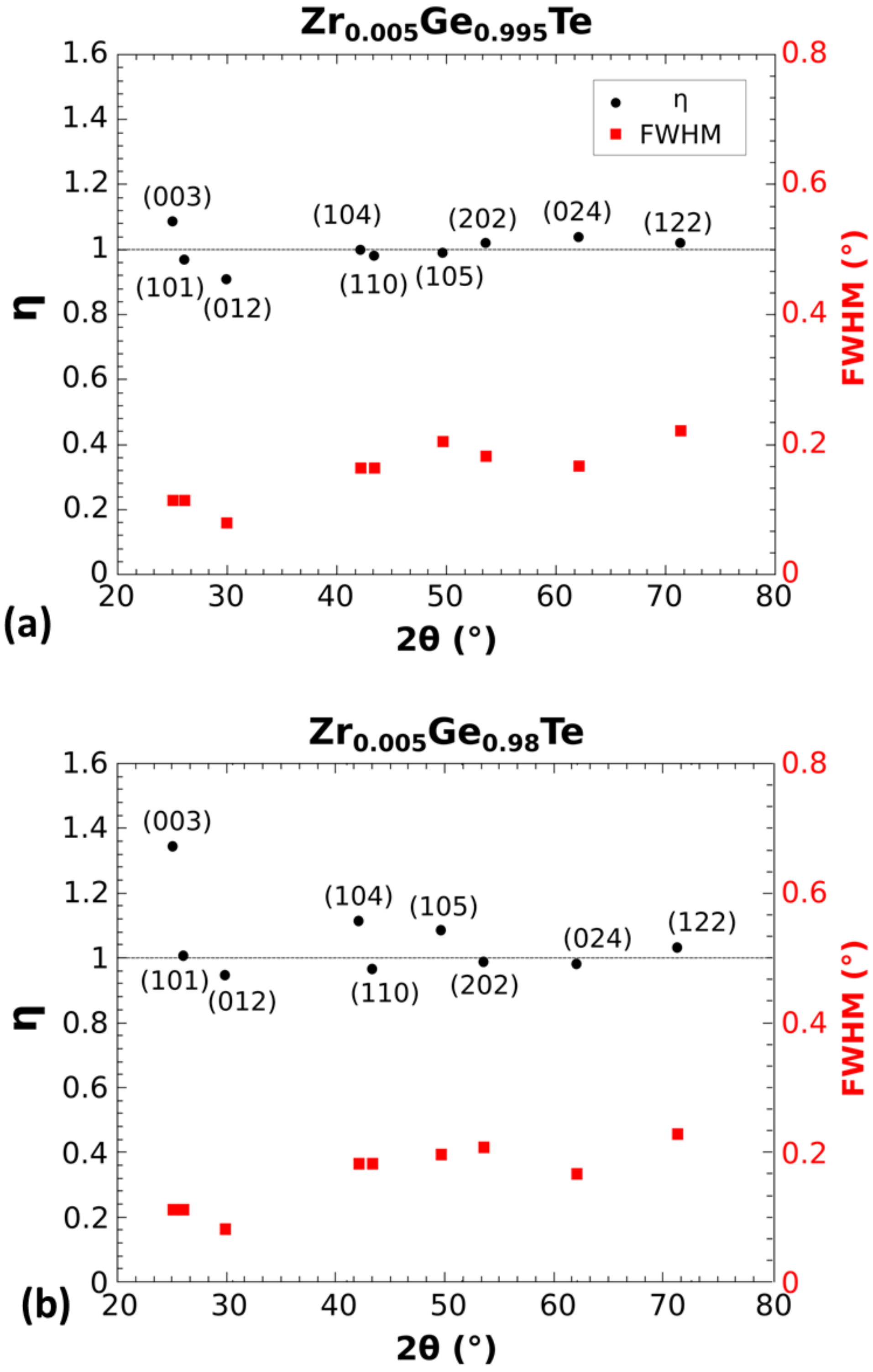

***Figure 11**. Refined η and FWHM obtained by individually fitting several Bragg peaks of stoichiometric (a) $Ge_{0.995}Zr_{0.005}Te$ and (b) Ge-deficient $Ge_{0.9}Zr_{0.005}Te$ diffraction patterns with a pseudo-Voigt function. The 'super-Lorentzian' profile with η significantly larger than 1 signifies the presence of a large density of planar defects in the Ge-deficient $Ge_{0.98}Zr_{0.005}Te$ compound.*

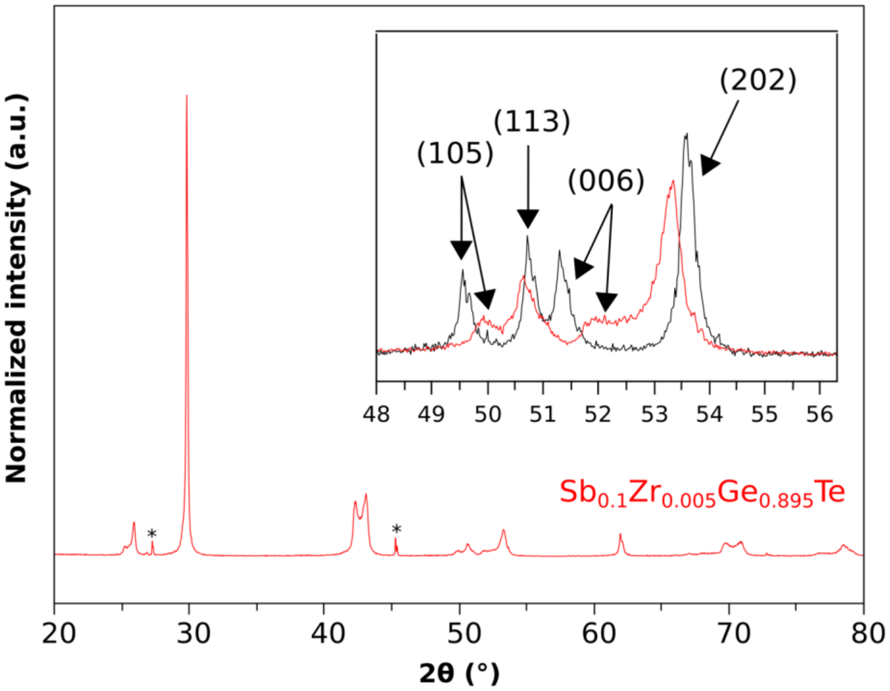

Figure 12: *PXRD pattern of Zr-Sb codoped $Ge_{0.88}Zr_{0.005}Sb_{0.1}Te$ compound. The inset is the magnified view of the $Ge_{0.88}Zr_{0.005}Sb_{0.1}Te$ (red) and $Ge_{0.98}Zr_{0.005}Te$ (black) patterns showing the peak shifts and broadening with the insertion of Sb in $Zr_{0.005}Ge_{0.995}Te$.*

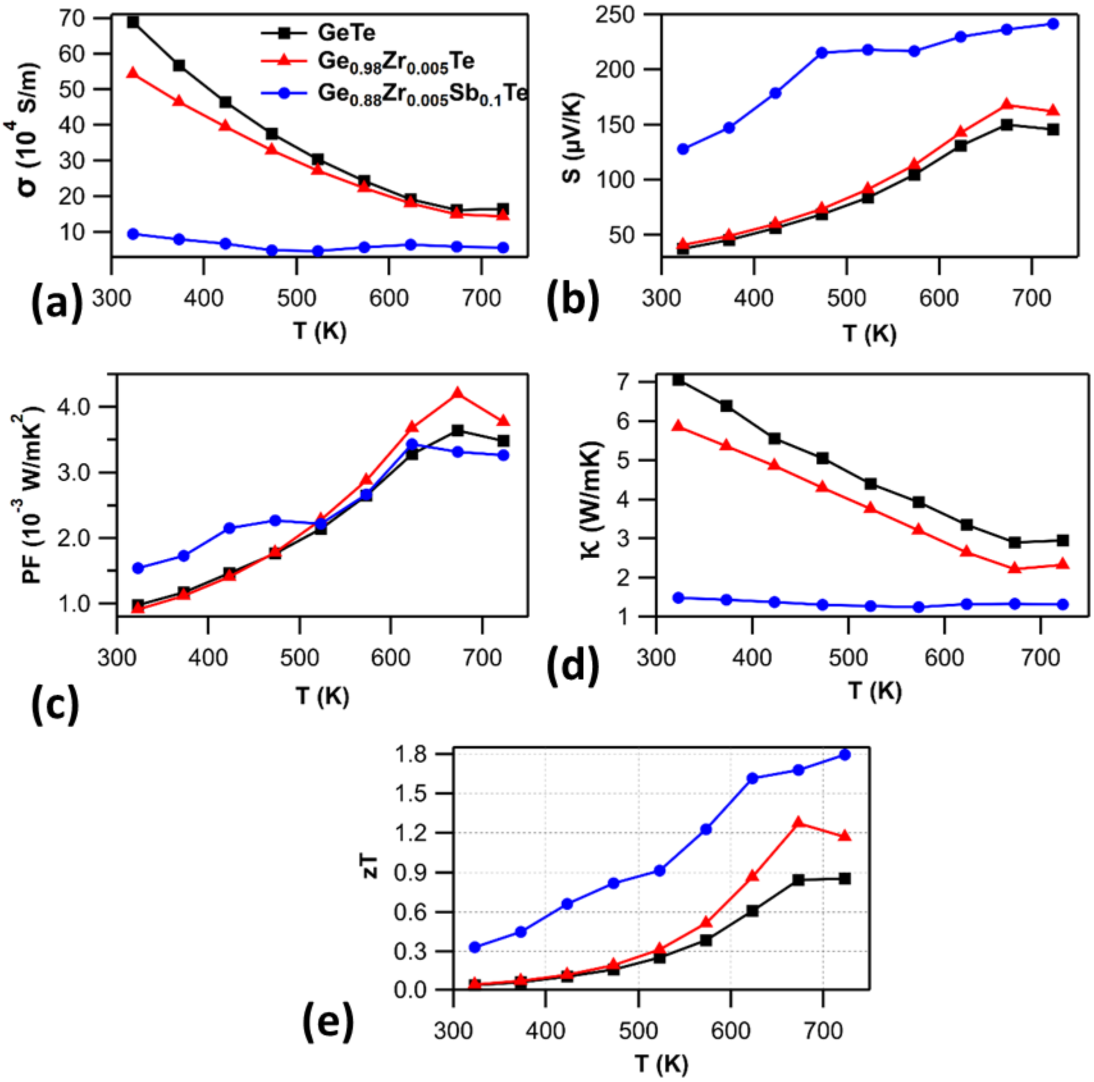

***Figure 13**. Temperature-dependent (a) electrical conductivity (σ), (b) Seebeck coefficient (S), (c) power factor (PF = $S^2\sigma$), (d) total thermal conductivity (κ), and (e) figure of merit (zT) for Zr-Sb codoped $Ge_{0.98}Zr_{0.005}Sb_{0.1}Te$ in comparison with Ge-deficient $Ge_{0.98}Zr_{0.005}Te$ and pristine GeTe.*

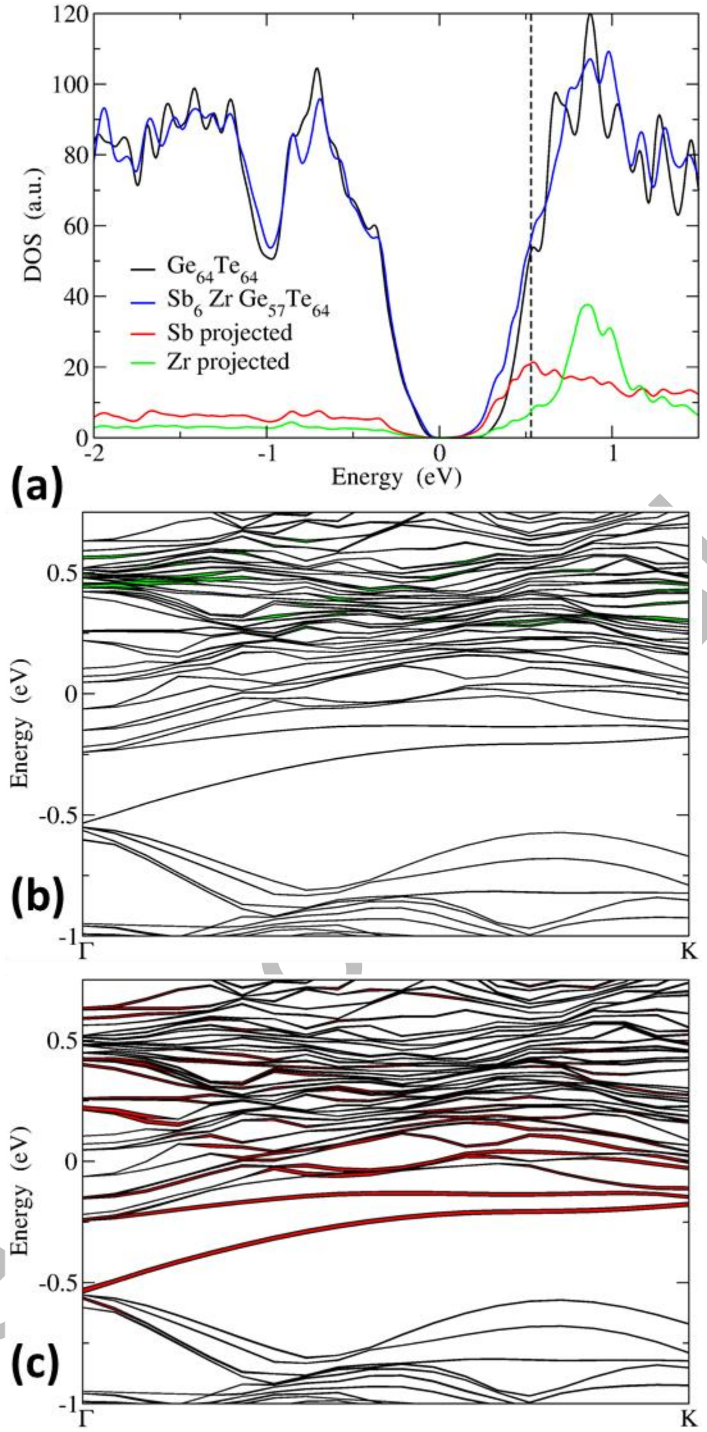

Figure 14. *First-principles computed DOS (a) and band structures highlighting (b) Zr projections (in green) and (c) Sb projections (in red) for the* $Sb_6ZrGe_{67}Te_{64}$ *cubic model. Additional figure captions (regarding* E_F*, additional Gaussian smearing, and projection of the wave function) given in Figures 4 and 5, apply also here.*

Table of Contents / Graphical Abstract

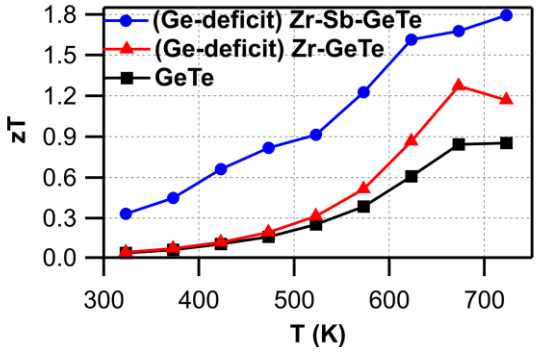

Reports an improvement in thermoelectric performance in GeTe via an intentional creation of more electrically dormant Ge-vacancies (in contrast to the classical approaches) and modulating/balancing it with optimized Zr-doping.